Nano Today 22 (2018) 14–35

Contents lists available at ScienceDirect

Nano Today

journal homepage: www.elsevier.com/locate/nanotoday

Review

Strain engineering in two-dimensional nanomaterials beyond graphene

Shikai Deng[a,b], Anirudha V. Sumant[b], Vikas Berry[a,*]

[a] Department of Chemical Engineering, University of Illinois at Chicago, 810 South Clinton Street, Chicago, IL, 60607, United States
[b] Center for Nanoscale Materials, 9700 South Cass Avenue, Argonne National Laboratory, Argonne, IL 60439, United States

ARTICLE INFO

Article history:
Received 16 December 2017
Received in revised form 14 June 2018
Accepted 18 July 2018
Available online 9 August 2018

Keywords:
Two-dimensional nanomaterials
Atomic sheets
Strain
Wrinkles
Anisotropic
Flexible devices
Heterostructures

ABSTRACT

Strain engineering is the process of tuning a material's properties by altering its mechanical or structural attributes. Atomically thin two-dimensional nanomaterials (2DNMs), which have been extensively studied in recent years, are particularly well-suited for strain engineering because they can withstand large strain. Thermal vibration, surface adhesion, substrate deformation, pre-stretched substrate, epitaxial grown, thermal expansion mismatch, substrate topography modification, pressurized blisters and tip indentation can lead to strain in 2DNMs. Strain in 2DNMs can modify their atomic structure, lattice vibration, thermal conductivity, electronic and optical, electrical and device performance, and chemical activities. This review focuses on the structural and mechanical properties of various 2DNMs, different experimental strategies to induce strain and modify properties, and applications of strained 2DNMs. Also, the review proposes prospective research areas for future strain engineering studies in 2DNMs.

Contents

* Corresponding author.
E-mail address: vikasb@uic.edu (V. Berry).

https://doi.org/10.1016/j.nantod.2018.07.001
1748-0132/

Introduction

The physical properties of most of the materials can be tuned over a wide range *via* strain engineering by mechanically shifting its structures (*e.g.* bond length, angle, and relative positions of atoms) [1–7]. However, because of the existence of the lattice defects in bulk three–dimensional materials, the low failure strains (about 0.1%) of bulk crystalline materials limit the extent to which their properties can be modified mechanically [8,9]. Two-dimensional nanomaterials are particularly promising candidates for strain engineering and related applications because they can withstand larger strain before rupture [10]. In 2DNMs, strain changes atomic bond-configurations (length, angles and strength), and the interaction between electronic orbitals, which in turn enables a control on the properties of 2DNMs providing a fertile library for advanced applications. For example, due to a unique combination of its crystallographic, electronic and chemical structure, graphene exhibits extraordinary properties [11]; and further, strain engineering in graphene can modify its electronic structure, create polarized carrier puddles, induce pseudomagnetic fields, and alter surface properties, which have been well investigated and summarized in previous studies and reviews [12–14]. Other 2DNMs (h-BN, phosphorene, transition metal dichalcogenide (TMDs), silicene, germanene and stanene) have been extensively studied in the recent decade. It is expected that strain engineering could also shed light on the modification of properties of 2DNMs beyond graphene. Here, we focus on several aspects of the strain engineering of these 2DNMs. Firstly, the atomic structure of these 2DNMs is different from graphene, which leads to different structural responses to the strain. We overview the atomic structures and mechanical properties (geometry structure, thickness, Young's modulus, tensile strength, Poisson's ration, and ultimate strain) of these 2DNMs. Further, the experimental methods and strategies for introduction of strain in 2DNMs are outlined, such as (a) intrinsic thermal ripples and lattice mismatch ripples, (b) thin film and rigid substrate interactions (mechanical exfoliation, epitaxial interaction and thermal expansion mismatch), (c) chemical doping and absorption, (d) bending and stretching of flexible substrates, (e) relaxation of pre-stretched substrates, (f) substrate surface topography modification, (g) pressurized blisters and tip indentation of suspended 2DNMs, and (h) piezoelectric substrate actuation. We also summarize the modification in structure, phonon vibrations, thermal conductivity, polarization, phase transition, electronic and optical properties, electrical and device performance, and chemical activity of 2DNMs by strain engineering. Finally, we discuss some important topics in the future research of the strain engineering of 2DNMs, such as strain responses of anisotropic 2DNMs, strain engineering in heterostructure structures of 2DNMs, 2DNMs with defects and strain engineering in other two-dimensional thin film materials.

Structure and mechanical properties of two-dimensional nanomaterials

Different from the defect-dominated response to strain in three-dimensional materials, the strain in 2DNMs is characterized by the modification of the atomic structure and mechanical properties of these atomic thin layers. Induced defects are certainly important in the strain engineering of 2DNMs [18–20]; however, that discussion is beyond the scope of this review, which covers only the strain in 2DNMs that does not cause lattice defects. The structure constants and mechanical properties of typical 2DNMs are summarized in Table 1. First, graphene is a well-studied 2DNMs, it is one atomic thick of carbon atom arranged in a honeycomb lattice [21]. Due to the hexagonal arrangement of carbon atoms, the graphene can be terminated with a zigzag edge and an armchair edge. Further, the edge structure, and termination play important roles in the properties of graphene. Theoretically, the thickness of the graphene is ~ 0.35 nm (the thickness of one layer of carbon atom in graphite) [22]. However, the value of thickness of graphene in the experiments is extended to much larger range (0.35 to 1.7 nm) [23,24]. Graphene is the strongest (measured) materials with a Young's modulus of ~1 TPa and a tensile strength of ~130 GPa [22]. Extensive studies have shown that the Poisson's ratio of graphene is ~0.165 [25]. However, recently, an investigation pointed out that the graphene experiences a transition from positive Poisson's ratio to negative Poisson's ratio (independent of its size and temperature) at high strain (above 6%) and this negative Poisson's ratio results from the interplay between bond stretching and bond-angle bending in graphene lattice under strain [26].

h-BN

h-BN is isostructural to graphene with boron and nitrogen atoms occupy the A and B sublattices of a 2D honeycomb lattice (so-called white graphene). The bond length of $B-N$ is ~1.44 Å, and that of $C-C$ in graphene is ~1.42 Å. Thus, the lattice mismatch between graphene and BN is small (~1.6 to 2%) [27,28]. h-BN is very planar, absence of dangling bonds, thermal and chemical inert with large bandgap (~ 6 eV), and small mismatch to graphene, which makes it one of the best substrate materials for the graphene electronics [29]. The thickness of monolayer h-BN is ~ 0.42 nm [30], with a theoretical thickness (interlayer spacing is ~ 0.33 nm). The in-plane Young's modulus is less than graphene, which is ~ 279.2 N/m (664.8 GPa) and Poison's ratio $\nu = 0.2176$. And the tensile strength is 8.8 ± 1.2 N/m (21.0 GPa), which is much smaller than its Young's modulus [31–33].

Phosphorene

Phosphorene is a two-dimensional nanomaterial of phosphorus atoms. Similar to graphene, monolayer phosphorene can be

Table 1
Summary of Structure and Mechanical Properties of the 2DNMs. Lattice constant, Thickness, Young's Modulus, Tensile strength, Poisson ration, Ultimate strain, Zigzag direction (Z), Armchair direction (A), Experimental studies (E) and Biaxial strain (B).

2DNMs	Structure	Lattice constant (nm)	Thickness (nm)	Young's modulus (GPa)	Tensile strength (GPa)	Poisson ratio	Ultimate strain
Graphene	Planar hexagonal	0.142 [29]	0.35 [23,24]	1000 [22]	130 [22]	0.165 [61]	0.25 [22]
h-BN	Planar hexagonal	0.144 [29]	0.42 [29,30]	665 [31]	21 [31]	0.2176 [31]	–
Phosphorene	Buckled hexagonal	0.33 [62]	0.5 [34]	166 (Z) [38] 44 (A) [38]	18 (Z) [38] 8 (A) [38]	0.62 (Z) [38] 0.17 (A) [38]	0.48 (Z) [38] 0.11 (A) [38]
Silicene	Buckled hexagonal	0.228 [63]	0.4 [41]	57 (Z) [43] 62 (A) [43]	6.0 (Z) [43] 7.2 (A) [43]	0.33 (Z) [43] 0.29 (A) [43]	0.19 (Z) [43] 0.175(A) [43]
Germanene	Buckled hexagonal	0.382 [45]	0.32 [45]	43.4 (Z) [43] 44 (A) [43]	4.1 (Z) [43] 4.7 (A) [43]	0.35 (Z) [43] 0.29 (A) [43]	0.205 (Z) [43] 0.2 (A) [43]
Stanene	Buckled hexagonal	0.48 [64]	0.35 [65]	23.5 (Z) [43] 25.2 (A) [43]	2.2 (Z) [43] 2.6 (A) [43]	0.42 (Z) [43] 0.36 (A) [43]	0.18 (Z) [43] 0.17(A) [43]
MoS_2	Three atomic layers hexagonal	0.312 [45,66]	0.65 [16,53]	222.75 (Z) [54] 219.46 (A) [54] 270 (E) [53,67]	27.35 (Z) [54] 16.90(A) [54]	0.25 [53,55]	0.28 (Z) [54] 0.19(A) [54] 0.11 (E) [51]
$MoSe_2$	Three atomic layers hexagonal	0.324 [54,66]	0.65 [68,69]	178.78 (Z) [54] 175.97 (A) [54] 177(E) [68]	22.68 (Z) [54] 12.86 (A) [54] 4.8 (E) [68]	0.23 [55]	0.29 (Z) [54] 0.16 (A) [54] – (E)
WS_2	Three atomic layers hexagonal	0.314 [54,66]	0.65 [53]	244.18 (Z) [54] 240.99 (A) [54] 272(E) [53]	29.96 (Z) [54] 19.91 (A) [54]	0.22 [53,55]	0.28 (Z) [54] 0.18 (A) [54] – (E)
WSe_2	Three atomic layers hexagonal	0.326 [54,66]	0.7 [70,71,72]	196.81 (Z) [54] 194.13 (A) [54] 167(E) [70]	24.70 (Z) [54] 15.05 (A) [54]	0.19 [55,70]	0.30 (Z) [54] 0.17 (A) [54] – (E)

produced by exfoliation of bulk black phosphorus. However, in a monolayer phosphorene, each phosphorus atom is covalently bonded with three adjacent phosphorus atoms to form a puckered honeycomb structure with notable non-planarity in the shape of structural ridges. The bulk lattice parameters are $a_1 = 3.36$ Å, $a_2 = 4.53$ Å. The thickness of the monolayer phosphorene is ~0.5 nm [34]. The quasi-two-dimensional puckered layer structure helps to keep orientation order between adjacent phosphorene monolayers and induces a strong anisotropy in phosphorene structure, as shown in Fig. 2a to d [34,35]. Therefore, the mechanical properties of phosphorene are found to be highly anisotropic and nonlinear. Specifically, the in-plane Young's modulus is 41.3 to 44 GPa in the direction perpendicular (armchair) to the pucker and 106.4 to 166 GPa in the parallel direction (zigzag). The ultimate strains are 0.11 and 0.48 in the armchair and zigzag directions, respectively [36]. The tensile strengths of monolayer phosphorene are up to 8 GPa and 18 GPa in the armchair and zigzag directions, respectively. Poisson's ratio in the zigzag direction ($\nu = 0.62$) are 3.8 times larger than their counterpart in the armchair direction ($\backslash\nu = 0.17$) [37,38]. Interestingly, to accommodate the tension in the plane, the puckered monolayer phosphorene expands in the out of plane direction under a tensile strain, which leads to a negative Poisson's ratio in the out of plane direction [39]. These unique mechanical properties of phosphorene in the two directions results from its puckered crystal structure (Fig. 2).

Buckled hexagonal crystal structure: Silicene, Germanene, and Stanene

Similar to carbon atoms, silicon, germanium, and tin atoms can also form 2DNMs with one layer of atoms arranged in hexagonal lattice. These 2DNMs corresponding to the Si, Ge or Sn are named (Xene) silicene, germanene, and stanene, respectively. However, bond lengths in these Xene (*e.g.* ~2.28 Å of silicene and ~3.82 Å of germanene) [40] are larger compared with graphene (~1.42 Å), which prevents these larger carbon family (Si, Ge or Sn) atoms from forming strong π bonds, thus leading to deviations from the sp^2 hybridization. Therefore, silicene, germanene, and stanene adopt buckled hexagonal honeycomb structures with two triangular sublattice-stacks, unlike graphene, which is planar (without considering the intrinsic ripples), as shown in Fig. 2e and f. To stabilize their hexagonal arrangements, the buckling of the Xene atoms brings them closer together to enable a stronger overlap of their π-bonding of p_z orbitals, resulting in a mixed $sp^2 - sp^3$ hybridization. The vertical buckling constant (Δ) (distance between the top and bottom atoms of the 2D-Xene crystal structure (Fig. 2f)) is related to the bond angle between the framework atoms and the hybridization of the atomic orbitals. Therefore, Δ in graphene is 0 Å, since it is planar with 120° of bond angle (pure sp^2 hybridization of C atoms), and Δ in freestanding stanene is up to ~0.85 Å, with almost pure sp^3 hybridization of Sn atoms [13]. The thicknesses of Xenes vary from 0.32 to 0.4 nm [41], as shown in Table 1. Xenes are mechanically anisotropic due to their anisotropic buckled 2D structures [42–45]. For example, an anisotropic Young's modulus (50.44 N/m for zigzag direction, 62.31 N/m for armchair direction) was determined in monolayer silicene; tensile strength on the order of 5.85 N/m and ultimate strain on the order of 18% of monolayer silicene.

Transition metal dichalcogenides (TMDs)

In structures of TMDs, each layer typically has a thickness of 0.6–0.7 nm, which consists of a hexagonally packed layer of metal atoms sandwiched between two layers of chalcogen atoms as shown in Fig. 1c and d [16,47]. The intra-layer metal (M) – chalcogen (X) bonds are predominantly covalent, the M—M bonds length varies between 3.15 Å and 4.03 Å, because of the size variation of the

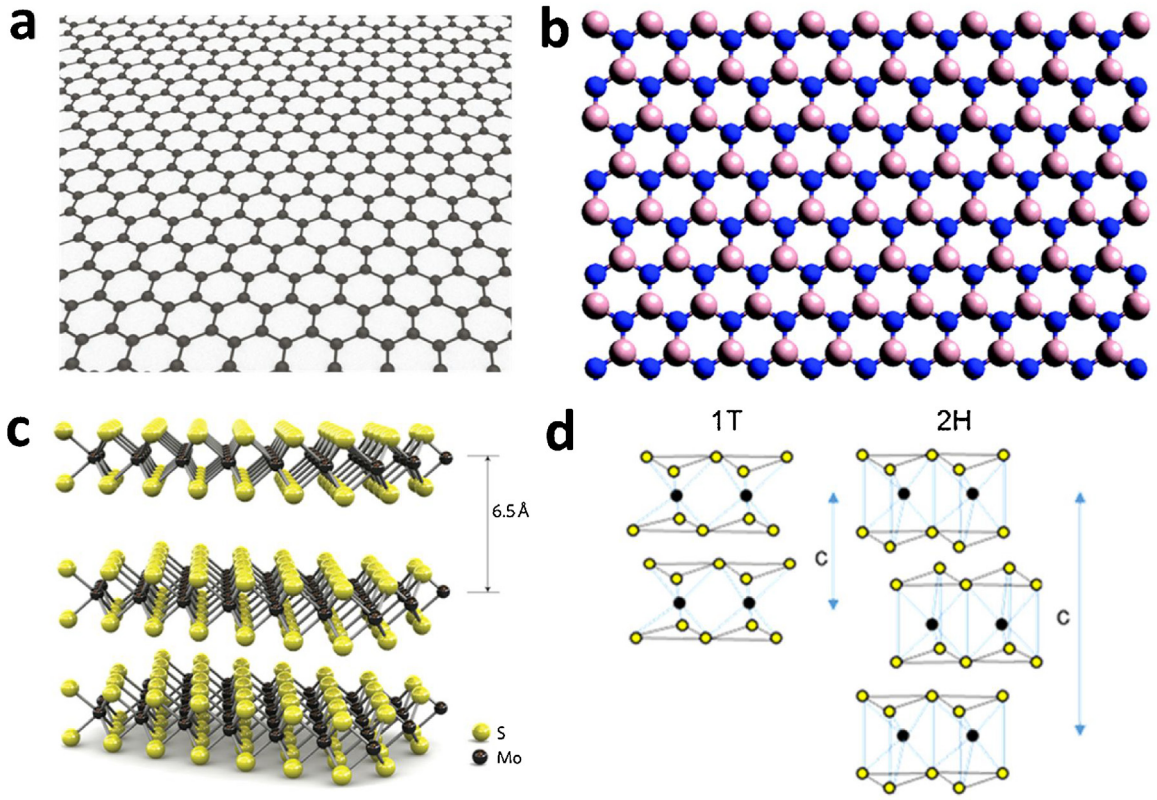

Fig. 1. Schematic of planar 2DNMs. Monolayer of graphene (a), h-BN (b), and MoS_2(c). (b) Adapted with permission. Copyright 2014, Royal Society of Chemistry [15]. (c) Adapted with permission. Copyright 2011, Nature Publishing Group [16]. (d) Side view schematic illustration of the 1 T/2H type structures of MoS_2. Adapted with permission. Copyright 2015, Multidisciplinary Digital Publishing Institute [17].

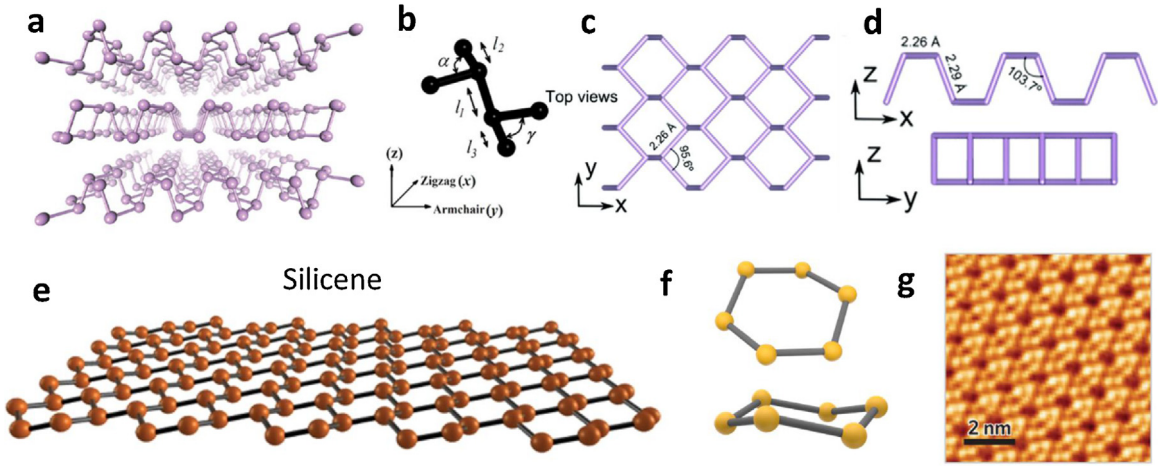

Fig. 2. Schematic of buckled 2DNMs. (a) Schematic of phosphorene; Adapted with permission. Copyright 2014, Nature Publishing Group [34]. (b) Atomic models of phosphorene; Adapted with permission. Copyright 2016, American Chemical Society [46]. Top view (c) and side view (d) of phosphorene. Adapted with permission, Copyright 2015, Royal Society of Chemistry [40]. (e) Schematic of a monolayer of silicene; Adapted with permission. Copyright 2015, Nature Publishing Group. (f) atomic models (bird's eye view and side view) of hexagonal ring of silicene; (g) High resolution STM image of silicene. (e) and (g) Adapted with permission. Copyright 2015, Nature Publishing Group [41].

metal and chalcogen ions. These bond lengths are 15–25% greater than the bond-lengths for elemental transition metal solids, revealing limited spatial overlaps of the d orbitals in TMDs. The lone-pair electrons of the chalcogen atoms terminate the surfaces of the layers, and the absence of dangling bonds makes those layers stable against reactions with environmental species. The sandwich layers are coupled by weak van der Waal's forces in bulk TMDs, thus allowing the crystal to readily exfoliate along the layer surface like graphite and bulk components of other 2DNMs [48]. MoS_2 is the most extensively studied TMD in recent years. It usually consists of a mixture of two major crystals of similar structures, so-called 2H (hexagonal) and 1 T (trigonal) phase as shown in Fig. 1d. The 2H phase of MoS_2 is more common and possesses semiconducting properties, however, the 1 T phase MoS_2 is metallic. Chemical lithium intercalation induces a phase change in MoS_2 from the 2H to the 1 T phase, and on the other hand, the 2H phase can transform from 1 T phase by annealing [49,50].

Experimentally, the in-plane Young's modulus of monolayer MoS_2 is 270 ± 100 GPa, with the average tensile strength of ~23 GPa and ultimate strain of ~ 11%. Poisson ratio of MoS_2 is 0.27 [51]. However, theoretically, the deformation and failure behavior are anisotropic. For example, calculations suggest that MoS_2 should undergo anisotropic nonlinear elastic deformation up to an extra-large ultimate strains: 0.24, 0.37, and 0.26 for armchair, zigzag, and biaxial deformation, respectively [52]. More anisotropic mechanical parameters of TMDs are shown in Table 1. Further, MX_2 (MoS_2 and WS_2, $MoSe_2$, WSe_2, and so on) have similar lattice constants and elastic properties from theoretical simulations [53,54]. In fact, strain-energy relationship of MX_2 monolayers from calculation has shown that the Young's modulus and tensile strength decrease when X changes from S to Te, and M changes from W to Mo. The calculated Poisson's ratios of TMDs monolayer are around 0.2 to 0.3, and the Poisson's ratio of TMDs along the zigzag direction is found to be larger than that along the armchair direction as shown in Table 1 [54,55].

It is important to mention that even values of mechanical properties along zigzag and armchair directions are anisotropic (theoretically); however, these anisotropic mechanical properties are not identified in most experimental studies [56–59]. Recently, it was shown that the bending rigidities of a single-layer MoS_2 is slightly higher along the zigzag direction than that along the armchair direction based on the analysis on two competition mechanisms (two-dimensional elastic modulus of monolayers and the structural relaxation of nanotubes). The relative trend in the magnitude of bending rigidities for different TMDCs is $MoS_2 < MoSe_2 < WS_2 < WSe_2$ [60].

Strain introduction methods in two-dimensional nanomaterials

Strain can exist in both planar and buckled (rippled, wrinkled and crumpled) 2DNMs. Buckled structures, out-of-plane deformation, are formed to relax a portion of the strain in 2DNMs. Compared to uniformly or locally distributed single strain (either tensile or compressive) in planar film, corrugations in 2DNMs contains spatially separated tensile and compressive strain simultaneously (*e.g.* tensile strain at the ridge and compressive strain at the valley of wrinkles). Here, we incorporate formation of bucked 2DNMs into methods of strain introduction, since the strain in these bucked 2DNMs has the same effect as the that of the strain in planar 2DNMs. Experimentally, the strain in 2DNMs are mostly induced through their interaction with substrates, since they are extremely thin and fragile to handle. Therefore, the interactions (strong adhesion in most cases) between 2DNMs and substrates are crucial for the strain engineering. Additionally, there are other methods to induce strain in suspended 2DNMs, like pressurized blisters method and tip indentation.

Intrinsic ripples

Similar to graphene, other suspended monolayer 2D crystals are expected to be unstable due to the thermodynamic requirement for the existence of out-of-plane bending with interatomic interaction generating a mathematical paradox [73,74]. The stability of the pseudo 2D materials is achieved by ripple formation resulting from the partially decoupled bending and stretching modes. Spontaneous ripples in MoS_2 was demonstrated experimentally and theoretically [75,76]. Small ripples with length $L \approx$ 6–10 nm, which corresponds to a ripple height $h \approx$ 6–10 Å are observed in mechanical exfoliated monolayer MoS_2. The typical ratio between the lateral ripple size L and their height h is ~10. The thermal fluctuated ripples also were predicted in the stanene monolayer at room temperature as shown in Fig. 3a. Due to the small Young's modulus of the stanene, the size of these thermally induced ripples in stanene are larger than the size of ripples in silicene and graphene (ripple size: graphene < silicene < stanene). [77]. Interestingly, for the phosphorene under strain, the small ripple and wrinkles only form in the zigzag direction but not in the armchair direction [78]. For the unsupported lateral heterostructure of 2DNMs, the lattice mismatch induced strain can be relaxed through out-of-plane ripples. However, on substrate supported heterostructure, this interfacial strain is relaxed by forming five-seven membered ring (graphene/h-BN interface) dislocation with small perpendicular penetration if the out-of-plane deformation is excluded [28,79,80].

Mechanical exfoliation

Because of their relative weak interlayer interaction (van deer Waals), 2DNMs can readily exfoliate to monolayer or thin layers by disrupting the interlayer interactions mechanically and/or chemically. In the mechanical exfoliation method, the interfacial adhesion force between samples and substrates pulls the MoS_2 sheets into intimate contact with substrates surface, 2D nanomaterials experience a separation from the bulk materials. During the release of the tape, its adhesion with 2DNMs on the substrate surface may lead to thin layers of 2DNMs partially delaminating from the substrate surface. In some cases, for mechanical equilibrium to be reached requires the 2DNM to contract to form the wrinkle as shown in Fig. 3b. The interplay between bending energy of the 2DNMs flakes and interfacial adhesion energy leads to the formation of wrinkles, and in turn, uniaxial strain in the 2DNMs flakes.

Epitaxial grown, thermal expansion mismatch, critical thickness and strain relaxation in heterostructures

Compared to the top-down exfoliation methods, bottom-up epitaxial and non-epitaxial growth methods (chemical vapor deposition (CVD) and molecular beam epitaxy (MBE)) can produce large-scale of 2DNMs on various substrates. A typical CVD growth process of 2DNMs includes substrate-surface reactions [85,86], sublimation, evaporation and/or reduction of solid metal precursors in reducer vapors (*e.g.* sulfur and selenium) [87]. On the other hand, high purity elemental precursors sublime and then condense (*e.g.* silicon) [41] or react (metals and selenium) [88–91] on the substrate surface in the MBE process. In bottom-up epitaxial processes, surface (chemical, lattice and topographic) properties of the substrate significantly affect the structure and properties of the 2DNMs grown on it. CVD is the most efficient and promising method to produce large area of 2DNMs [92–94]. Because of different thermal expansion coefficients and lattice constants of substrates and 2DNMs, non-uniform and localized strain (lateral) is expected to build-up on the 2DNMs during the CVD process. Heteroepitaxy grown thin films are strained up to a critical layer thickness (order of a few nanometers) [95–97]. In the case of the heterostructure of the 2DNMs, two different interfaces exist: a two-dimensional interface for vertical heterostructure and one-dimensional interface for lateral heterostructure. The critical thickness in both vertical and lateral heterostructures depend on the lattice constant mismatch at the interface with the larger critical thickness expected for higher lattice mismatch. However, different from their three-dimensional counterparts, the two-dimensional thin film can form out-of-plane deformations to relax the interfacial strain without the introduction of dislocations. In some cases, the interfacial strain relaxes at the one-dimensional interface with short penetration distance *via* the formation of misfit dislocations as shown in Fig. 3e. The interfacial strain, as well as the thickness of the relaxation layer, also depends on the other interfacial properties, like interface defect

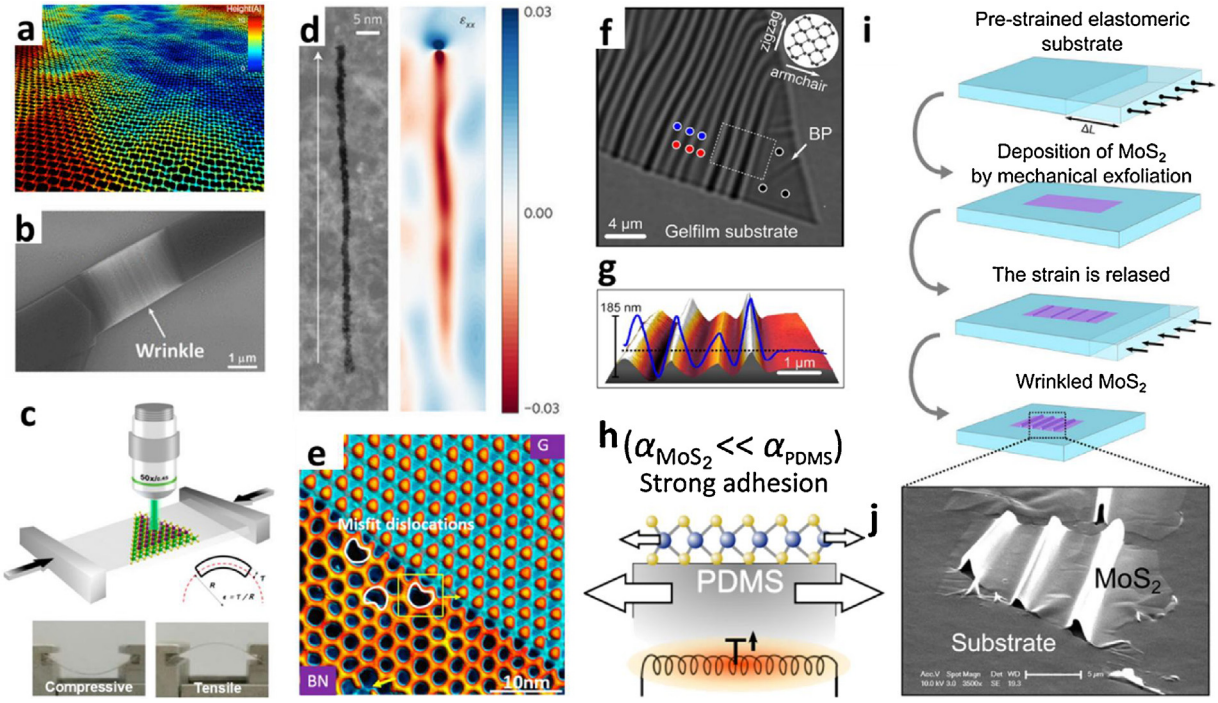

Fig. 3. Strain introduction in 2DNMs. (a) Ripples in monolayer stanene caused by thermal fluctuations. Adapted with permission. Copyright 2016, American Chemical Society [77]. (b) SEM image of MoS_2 wrinkles on SiO_2 by mechanical exfoliation method. Adapted with permission. Copyright 2017, American Chemical Society [81]. (c) Schematic of substrate bending for compressive and tensile strain introduction to WS_2/MoS_2 vertical heterostructure. Adapted with permission. Copyright 2017, American Chemical Society [82]. (d) STEM image (left) and its strain map (right) of a MoS_2 1D channel formed from an intrinsic 5|7 dislocation in WSe_2. Copyright 2017, Nature Publishing Group [83]. (e) Magnified STM image of misfit disorder at graphene/BN boundary. Adapted with permission. Copyright 2014, American Chemical Society [28]. (f) Transmission-mode optical image of a ripples 10 nm thick black phosphorus flake. The inset is a sketch of the crystal lattice orientation. (g) Atomic force microscopy topography image for the dashed line rectangular region in (f). (f) and (g) Adapted with permission. Copyright 2016, American Chemical Society [57]. (h) Schematic of the thermal expansion mismatch experiments with MoS_2 on SiO_2 (f) and PDMS substrates (g). Adapted with permission. Copyright 2015, IOP Publishing Ltd [84]. (i) Schematic of prestretched substrate method, and (j) a SEM characterization results of wrinkled MoS2 on substrata. Adapted with permission. Copyright 2013, American Chemical Society [56].

and inter-weak layer. The high defect-density and large relaxing ability of interlayer are expected to reduce the lattice-mismatched interfacial strain and critical thickness [28,79,80].

Since the thickness of single and few atomic layers of the 2DNMs are below the critical thickness, interfacial strain cannot be completely compensated by the formation of the misfit dislocation in the vertical heterostructure of 2DNMs [97,98]. Compressive strain accumulates in the MoS_2 film when it stacks on carbon because of the lattice-mismatched carbon-MoS_2 interface. Base on this phenomenon, large-scale bucked MoS_2 thin films were produced by treating molybdenum metal thin films on CVD graphene covered on the SiO_2 surface in the sulfur atmosphere [99]. Additionally, pre-patterned sapphire substrates were interfaced with bilayer MoS_2 during epitaxial growth for *in situ* introduction of the compressive strain. The magnitude of strain could be controlled by modifying the geometric shape of the protuberance (cone and pyramid) [100]. Similarly, the large scale of tensile strain in the MoS_2 thin film interfaced with a SiO_2 substrate with anisotropic patterns was also reported [101,102]. Tensile strains in CVD-grown MoS_2 and WS_2 on SiO_2 can be released after transferring to new substrates [103]. Further, strain-free MoS_2 can be synthesized on epitaxial graphene on SiC, due to the strain relaxation in the van der Waals gap [100–102,104]. An experimental study on one-dimensional (lateral) heterostructure was recently reported by Xie et al. Different TMD monolayer-superlattices, repeated and laterally integrated were produced by precisely controlling respective precursors in the CVD process. Tensile strain due to lattice mismatch between WS_2 and WSe_2 at the interfaced led to ripple formation. The magnitude of the strain was tuned by the relative width between WS_2 and WSe_2 lattices. These ripples in WSe_2 transitioned from continuous to discontinuous with the width of the WSe_2, attributed to the strain relaxation (misfit dislocations). The abnormal coherence length (~320 nm) may be caused by a combination of the lattice and substrate mismatch [105].

Chemical doping and absorption

Compressive strain can be introduced by a decrease of lattice constant with incorporation of smaller atoms into 2DNMs. After exposing of MoS_2 in N_2 plasma, chalcogen sulfur atoms in MoS_2 were substituted by nitrogen. Mo-N bond was compressive causing contraction of the MoS_2 lattice, which was evidenced by the blue-shift of the E^1_{2g} peak and crack-formation [106]. Hydrogen intercalation of sulfur vacancies in MoS_2 was reported to induce tensile strain in MoS_2 lattice [107].

Deformation of flexible substrates

2DNMs have been transfered onto flexible substrates (PMMA, PDMS, PET and Polycarbonate) for bendable electronics applications. By applying tensile stress or compressing on the two side of the substrates (Fig. 3c), 2DNMs experience the strain similar to that experienced by the substrate, assuming there is no relative slip [59]. For example, in one work MoS_2 thin films were mechanically exfoliated and deposited onto a layer of cross-linked SU-8 photoresist covered polycarbonate. Titanium clamps were then evaporated to prevent MoS_2 from slipping against the substrate. Uniaxial strain was applied to MoS_2 by controllably bending the polycarbonate substrate in a four-point bending apparatus [58,108]. Additionally, similar to the graphene wrinkle-engineering, 2DNMs thin film was transferred on the pre-stretched substrates. The release of uniaxial tension in the elastomeric substrate enabled formation

of well-aligned one-dimensional periodic wrinkles in the 2DNMs. This method reproducibly generates large-scale wrinkles (micrometers in height, separated by tens of micrometers) for thick MoS_2 flakes (more than 10–15 layers), while thin MoS_2 layers (3–5 layers) exhibit wrinkles that are between 50 and 350 nm in height with wavelength of few micrometers (Fig. 3i and 3 j) [56]. Same method was employed to study the strain effect in black phosphorus, where the experiments and characterizations were conducted in short period of time to avoid degeneration of black phosphorus, as shown in 3f and 3 g [109]. Here, the size of the wrinkles can be controlled by tuning different parameters, like, the Young's modulus of the substrate, thickness of the thin film, and the interfacial adhesion between the thin film and substrate. In another process, MoS_2 on heated PDMS substrate causes thermal expansion of the MoS_2; however, due to its larger thermal expansion coefficient, the PDMS substrate can induce an additional biaxial strain in MoS_2 as shown in Fig. 3h. In comparison, smaller strain is induced in the reference samples with MoS_2 on SiO_2, which is due to the smaller thermal expansion coefficient of SiO_2 and smaller thermal expansion mismatch between MoS_2 and SiO_2. Laser beam can also be applied as a heat source to induce local heating and regionally controlled strain in the MoS_2; however, the maximum strain achieved by this method is small (~0.2%) [84].

It should be noted that the magnitude of the strain in the substrate is not necessarily equal to the strain in the 2DNMs on the strained substrates. To achieve high strain transfer efficiency from the substrate to the 2DNMs, the interfacial separation or sliding must be eliminated. In most substrate bending experiments, two side of 2DNMs were anchored on the substrate, therefore, the tensile strain in 2DNMs is relative close the strain in substrate (transfer efficiency ~ 1) [110]. Without this substrate-film anchor, the strain transfer efficiency would significantly reduce, like ~ 12% in WS_2 on PDMS experiment [111]. Further, strain relaxation (wrinkles and cracks) formed under high strain can further reduce the strain transfer to 2DNMs from substrate [111].

Substrate surface topography modification

2DNMs are very thin (1–3 atomic layers), which means they are flexible enough to conform to most surface morphologies of the substrate under them. The relative strong interfacial adhesion energy between 2DNMs and substrate surface leads to strain accumulation near the protruding features on the substrate surface [112]. Therefore, the strain in the thin 2DNMs can be manipulated by tuning the attributes of these protruding feather (size, height, density, and shape). One of the examples is 'artificial atom', which is transferring a monolayer of CVD produced MoS_2 on nanocones on the surface as shown in Fig. 4a and b. The roughness of the substrate under 2DNMs plays an important role in the strain formation in the 2DNMs [81,113]. The local topographic curvature induced strain were also shown in exfoliated MoS_2 on gold nanoplates [114] and CVD grown monolayer MoS_2 films on 3D nanoporous gold [115].

Pressurized blisters, blown-bubble and tip indentation

The pressurized blisters method to study strain in 2DNMs was introduced by Bunch's group [116]. Mechanically exfoliated or chemical vapor deposited graphene or MoS_2 was transferred on pre-defined microcavities in oxidized silicon wafers (Fig. 4d to f) [116,117]. Because of the excellent gas molecular impermeability of 2D nanomaterials, sealed micro cavities were formed. Samples were left in the pressure chamber at P_0 (outside pressure) for couples of days to make sure P_{int} (pressure inside the sealed micro cavities) equilibrates with P_0 through the slow diffusion of gas through SiO_2 substrate. The pressure difference ΔP between the environment (out of sealed micro cavities) P_{ext} and microcavities P_{int} deformed the 2DNMs and induced strong tensile strain in these thin films when the samples were place in a different pressure chamber (P_{ext}). These pressurized graphene blisters were also applied to measure the adhesion energy between 2DNMs and silicon dioxides surface [116,118]. The strain here is biaxial and relatively large (up to 5%) [116,117]. Similarly, MoS_2 thin film was first transferred to and clamped on a PDMS substrate, the substrate was bulged into bubble by supply higher gas pressure under it. The strain was introduced to MoS_2 thin film by the curved PDMS substrate (Fig. 4g). Comparing to the pressure blister method, this "blown-bubble" PDMS technique is vacuum free and facilitated for flexible device application [119]. Further, mechanical strain can also be introduced in 2DNMs by atomic force microscope tips loading on suspended 2DNMs thin film (over two metal contacts or holes as shown in Fig. 4c). This method is good for investigation of the mechanical properties of 2DNMs, like measurement of the Young's modulus and tensile stress. However, it may not be practical for device application [51,67,75].

Piezoelectric substrate actuation

Ding et al. reported on the application of a piezoelectric film (1-x)[$Pb(Mg_{1/3}Nb_{2/3})O_3$]-x[$PbTiO_3$] (PMN-PT) as a substrate for introduction of tunable biaxial stress in graphene. A bias voltage applied to the PMN-PT results in an out-of-plane electric field, which leads to an in-plane strain, allowing for a smooth variation of strain (biaxial compressive or tensile) in graphene [120]. A similar setup has been applied to study the effect of strain on phonon vibration and photoluminescence in CVD-grown trilayer MoS_2, as shown in Fig. 4h. To maximize the strain transferred from the PMN-PT substrate onto MoS_2 thin films, graphene was transferred as a top transparent electrode for voltage supply [108]. The advantage of this method is the applied voltage can continuously tune tensile and compressive strain; however, a high voltage is needed even for a relatively small strain (0.2%/500 V).

Modification of properties and applications

Lattice structure, phonon vibration and thermal conductivity

The strain in 2DNMs introduces changes in the bond lengths and angles, and in some cases, lattice deformations. This structure modification under strain, in turn, leads to a considerable change in the lattice vibration (phonon), and this phonon frequency shift can be detected in Raman spectroscopy (Fig. 5a). Under biaxial strains (−2% to 18%), the frequency of in-plane vibration modes in h-BN goes up and the out-of-plane vibration frequency decreases almost linearly. The effect of strain on the frequency of the in-plane vibration modes is larger than that of the out-of-plane vibration modes [121]. When the uniaxial tensile strain is applied along the zigzag direction of MoS_2, the bond lengths along the zigzag direction increases with strain gradually, but the bonds along the armchair direction decrease with strain, and further bond angle change, resulting in lattice distortion. Additionally, the initial structure of the monolayer MoS_2could be maintained and no structural transformation takes place at a large biaxial strain (up to 22%), but imaginary frequencies appear near Γ points when the strain is increased up to 25%, indicating structural instability and possible structural transformation [122,123]. Theoretically, the phonon mode shifts of the A_{1g} mode (out-of-plane) in MoS_2 is not sensitive to the uniaxial strain, even when the uniaxial strain is increased up to 20% in monolayer MoS_2, but it decreases significantly under biaxial strain. The frequency of the E^1_{2g} modes shows an obvious redshift under uniaxial and biaxial tensile strain, since it is due to in-plane phonon vibration. Further, the asymmetrical shift of S-

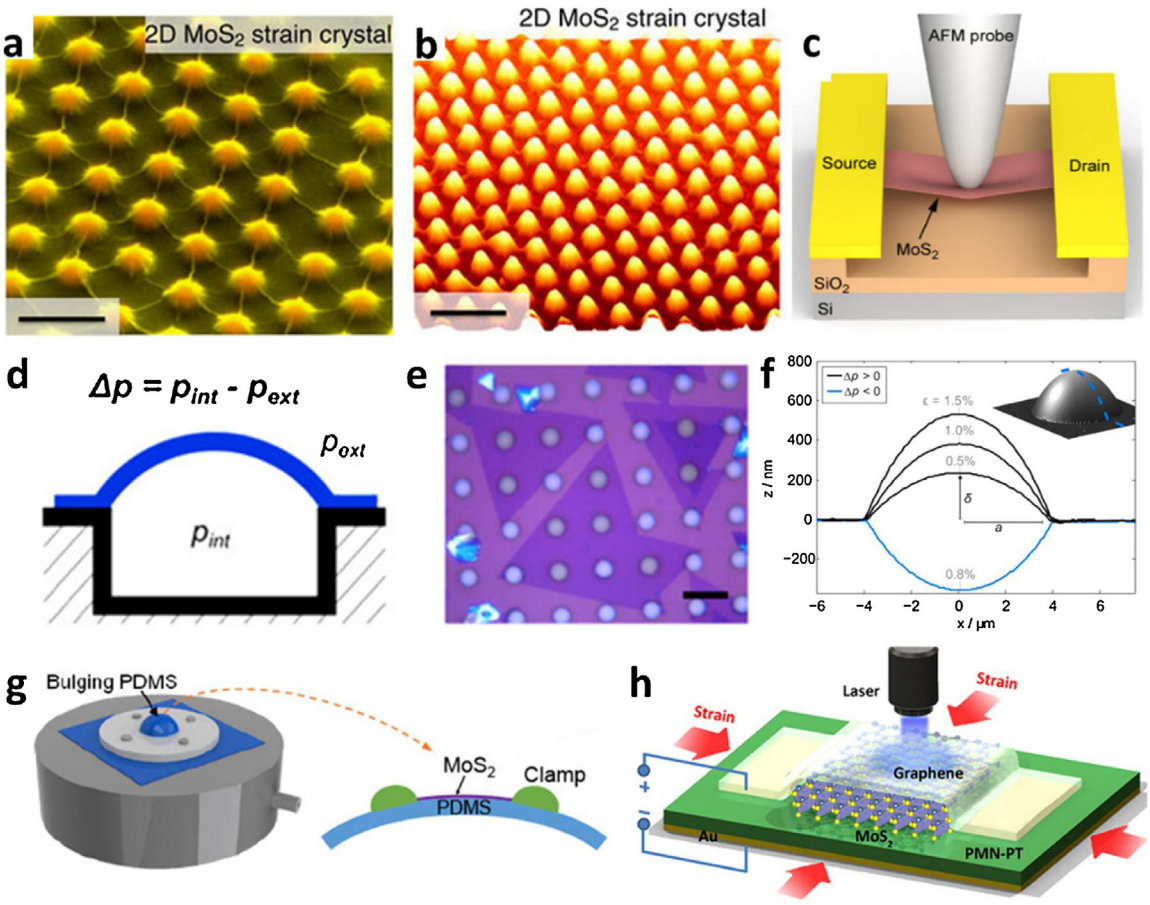

Fig. 4. Strain introduction in 2DNMs. (a) Tilted false-color SEM image of the 2D strained MoS_2 crystal by the nanocone array substrate surface modification. Scale bar is 500 nm; and (b) AFM topography of the 2D MoS_2 strain crystal. Scale bar is 1 mm; Adapted with permission. Copyright 2015, Nature Publishing Group [113]. [67]. (d) Schematic (d) and optical image (e) of pressurized blisters. (f) A side view of AFM measurements for pressurized blisters at different pressures, MoS_2 layer can be bulged up or down depending on whether Δp is positive or negative. (d) to (f) Adapted with permission. Copyright 2016, American Chemical Society [117]. (g) Schematic illustration of the experimental setup of blown-bubble bulge measurement. Adapted with permission. Copyright 2017, American Chemical Society [119]. (h) Schematic illustration of configuration of our electromechanical strain introduction device. Adapted with permission. Copyright 2013, American Chemical Society [108].

Mo-S bond in MoS_2 lattice under uniaxial strain induces a splitting of vibration frequency at point Γ, which leads to the E^1_{2g} mode splitting into two modes [124]. This frequency splitting does not occur under the biaxial strain up to 5%, since the lattice symmetry is maintained in this case [117]. Further, both theoretical and experimental results have shown that the shift in the positions of Raman modes in MoS_2 linearly depends on applied strain (~-5 to $-2\,cm^{-1}/\%$), therefore, the strain in MoS_2 can be quantified in Raman spectrum [117,119]. The E^1_{2g} peak of bilayer WSe_2 splits to E^{1-}_{2g} (phonon mode along the strain direction) and E^{1+}_{2g} (phonon mode perpendicular to the strain direction) under strain. The redshift of the E^{1-}_{2g} peak indicates the existence of tensile strain in the strain direction and the blueshift of E^{1+}_{2g} peaks shows compressive strain in the perpendicular direction of strain, as shown in Fig. 5c. This opposite direction of the shift can enable the measurement of Poisson's ratio based on this strain effect [125]. Moreover, the E^1_{2g} Peak of WS_2 showed a linear dependence (redshift on tensile strain and blueshift on compressive strain) on the strain, as shown in Fig. 5d and e [82,111]. The shift in Raman modes shows a clear anisotropy with respect to the crystallographic direction of applied strain in phosphorene, as shown in Fig. 5f [82]. The redshift of Raman B_{2g} mode is significant (~ $-11\,cm^{-1}/\%$) when the uniaxial tensile strain is aligned in the zigzag direction, which is larger than the shifts of A^1_g mode (~ constant) and A^2_g mode (~ $-4\,cm^{-1}/\%$) in the same strain direction. For uniaxial strain along an armchair direction, A^1_g mode shift ~ $-4\,cm^{-1}/\%$, however, A^2_g and B_{2g} modes stay relatively unchanged. This anisotropic Raman-strain response can facilitate the determination of the crystallographic orientation in phosphorene [126]. A similar trend is observed for the uniaxial strain in the near-zigzag and near-armchair directions [127]. This extraordinarily anisotropic response of Raman shift is attributed to the directional-differences in the change of bond-length and bond-angle in strained phosphorene.

The lattice constants in silicene and germanene increase under tensile strain. As tensile strain increases from 0 to 5%, the buckling constants (Δ) decreases from 0.44 to 0.24 Å in silicene and 0.64 to 0.60 Å in germanene. The decrease in the buckling constant in germanene is much smaller than that in silicene for the same strain range, due to the different atomic radius of Si (~1.09 Å) and Ge (~1.22 Å). The larger atomic radius makes the Ge-Ge bonds less sensitive to a relatively small strain than Si-Si bonds [128,129]. The Raman characterization for response of silicene and germanene to strain are still under investigation, since the silicene and germanene are unstable in ambient environment.

In general, a tensile strain can lead to a reduction in the thermal conductivity of nanomaterials, due to the softening of the phonon modes [131]. Both experimental and theoretical studies showed that MoS_2 under tensile strain displays an obvious redshift in the in-plane phonon peaks and a positive Grüneisen parameter, indicating a reduction in thermal conductivity of monolayer MoS_2 with tensile strain [58]. This strain-dependent thermal conductance has also been shown in phosphorene *via* a theoretical study [130]. Thermal

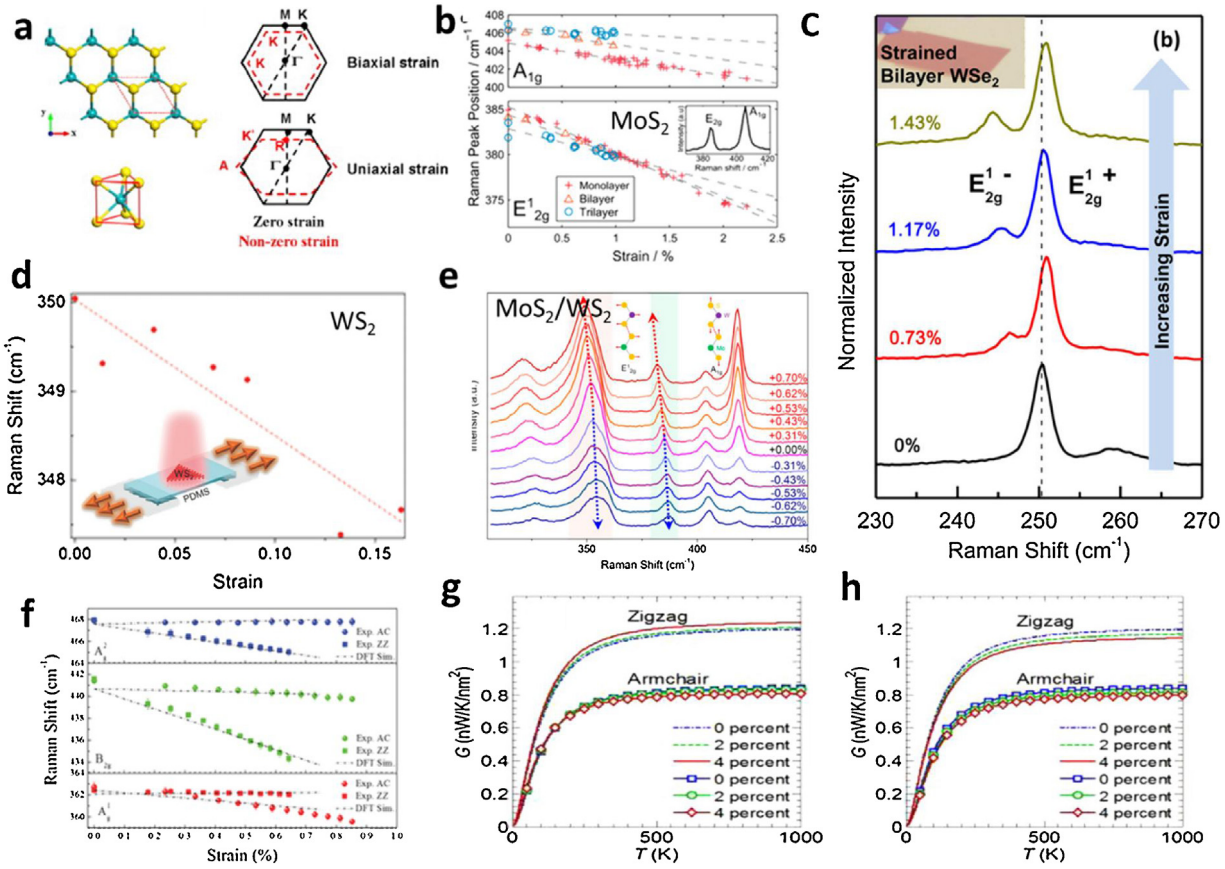

Fig. 5. Strain effect on phonon vibration and thermal conductivity in 2DNMs. (a) atomic models and the unit cell of monolayer MoS_2. The x and y axes correspond to the zigzag and armchair directions, respectively. The change of Brillouin region in reciprocal space under biaxial tensile strain and uniaxial tensile strain. Adapted with permission, Copyright 2015 Elsevier B.V [122]. (b) The $E^1{}_{2g}$ and A_{1g} Raman modes for MoS_2 peak positions as a function of biaxial strain for different membrane thicknesses. Adapted with permission. Copyright 2016, American Chemical Society [117]. (c) Raman spectra of bilayer WS2 under strain; Adapted with permission. Copyright 2014, American Chemical Society [125]. (d) WS_2 $E^1{}_{2g}$ peak position at different strain (PDMS strain with strain transfer efficiency about 12% to WS_2). Insert is the schematic illustration of the PDMS stretching for strain introduction in WS2. Adapted with permission, Copyright 2016, WILEY-VCH Verlag GmbH & Co. KGaA, Weinheim. [111]. (e) Evolution of the Raman spectra of WS_2/MoS_2 vertical heterostructure; Adapted with permission. Copyright 2017, American Chemical Society [82]. (f) Experimental and calculated evolution of the Raman spectra of phosphorene under strain aligned in zigzag and armchair directions. Adapted with permission, Copyright 2016, WILEY-VCH Verlag GmbH & Co. KGaA, Weinheim. [126]. (g) zigzag and (h) armchair direction in phosphorene. Adapted with permission. Copyright 2014, American Chemical Society [130].

conductance reduces with biaxial strain in phosphorene, however, a significant and unusual crystallographic orientation-dependence of thermal conductance is observed under uniaxial strain, because of its strong anisotropic buckled atomic structure. The room-temperature thermal conductance along the zigzag direction is 40% higher than that along the armchair direction without strain (the anisotropic ratio zigzag/armchair is 1.4). The zigzag-oriented thermal conductance is enhanced when a zigzag-oriented strain is applied but decreases when an armchair-oriented strain is applied. On the other side, the armchair-oriented thermal conductance always decreases when either a zigzag- or an armchair-oriented strain is applied. The anisotropy ratio is insensitive to the armchair-oriented strain, but increases with the zigzag-oriented strain, from 1.4 to 1.6 under 5% tensile strain (Fig. 5g to h). It is expected that strain engineering may open a new way for the design of novel thermal devices based on this anisotropic thermal conduction and anisotropic strain responses in phosphorene [130].

In addition to the well-known effect of strain on thermal conductivity in materials, it is interesting to mention the dependence of interfacial thermal resistance on strain for different types of materials. The interfacial thermal resistance increases with tensile strain, which could be attributed to the different atomic masses induced different strain shift rates and response at the interface. The strain in 2DNMs enhances the mismatch between phonon vibrations at interface and leads to the increase of interfacial phonon scattering and thermal resistance, which may be important for 2DNMs heterostructures [132–134].

Structure, polarization and phase stability

Under strain, the substrate supported 2DNMs are stable because of interaction with substrates. Liang et al. have shown that interlayer van der Waals force is strong enough and no interlayer sliding during the bending of the substrate in bilayer $MoSe_2$ (up to 1.3% uniaxial strain) [110]. However, strain induced wrinkles for strain relaxation was observed under higher strain in WS_2 thin film (2–3% uniaxial strain) [111]. This strain induced out-of-plane deformation is energy favorite for strain relaxation in free standing 2DNMs [79]. Besides the lattice vibration and structure, the polarization and phase properties are closely linked to the lattice symmetry and are expected to be modified with the application of mechanical strain. For example, the strain dramatically affects the polarization degree in MoS_2. When the strain is increased up to 0.8%, the PL polarization degree decreases 40% (from 10% to ~ 6%) in monolayer and ~ 100% (6% to ~ 0) in bilayer MoS_2, as shown in Fig. 6a and b [123]. TMDs can exist in multiple crystal structures, each with distinct electrical properties, and the two lowest energy crystal structures are often referred to as H and T [135–137]. The H phase is a semiconducting phase with for all Mo and W-based TMDs photon adsorption bandgap between 1 and 2 eV at ambient conditions. The semi-

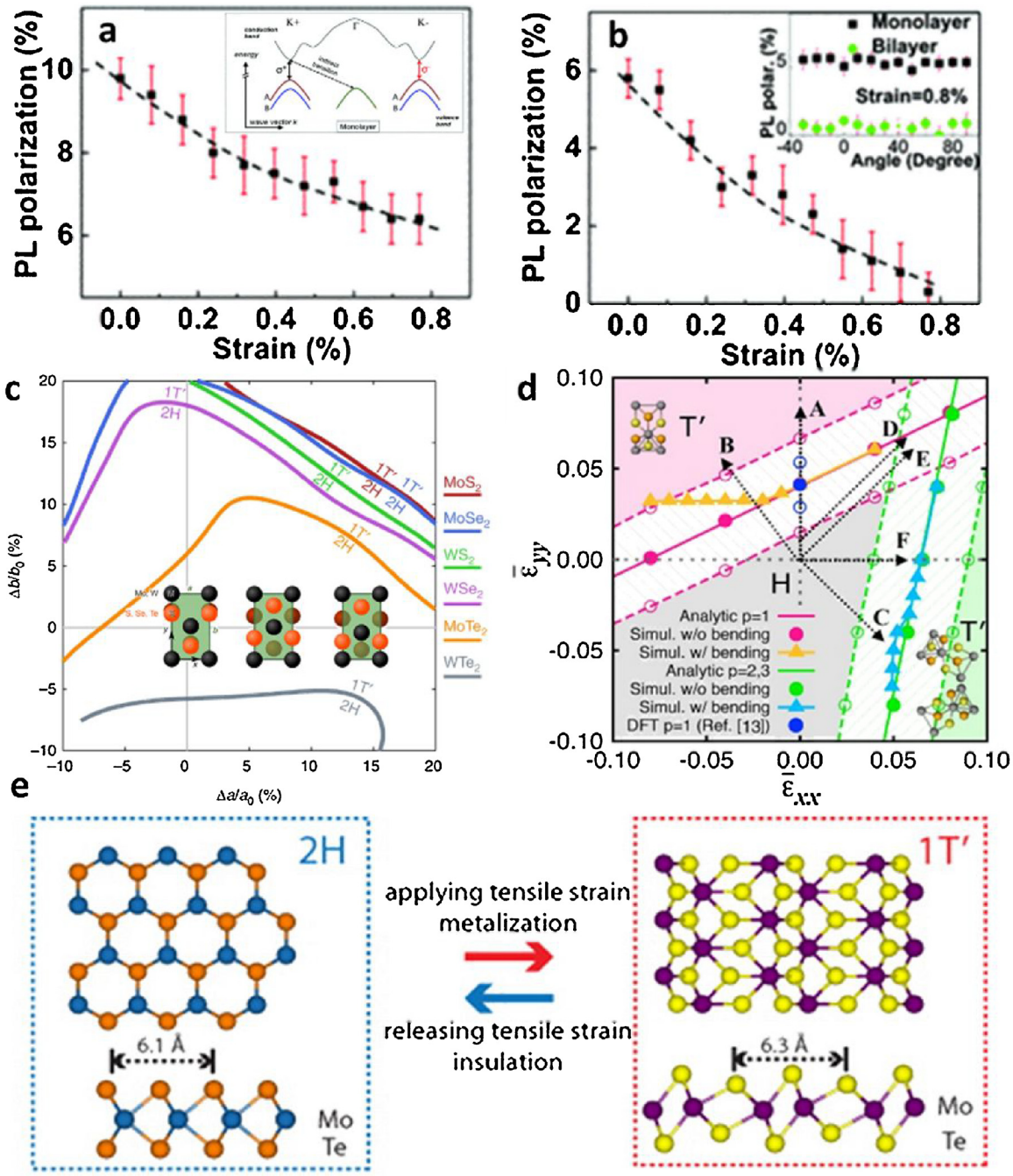

Fig. 6. Structure, polarization and phase stability under strain. PL circular polarization degree as a function of the applied tensile strain for monolayer (a) and bilayer (b) MoS_2; Insert in (a) is a scheme of the band structure for monolayer MoS_2 at zero strain and insert in (d) is PL polarization measured as a function of the angle of the applied strain to the in-plane crystal orientation under a 0.8% of strain. Adapted with permission, Copyright 2013 American Physical Society [123]. (c) Phase transition of TMDs under strain, and the insert is the three phase structures of some typical TMDs. Adapted with permission. Copyright 2014, Nature Publishing Group [136]. (d) Transformation morphologies in $MoTe_2$ under an in-plane strain. Adapted with permission. Copyright 2017, American Chemical Society [141]. (e) Atomic structures of 2H and 1 T′ $MoTe_2$. Polymorph of $MoTe_2$ is controlled by in-plane tensile strain., Adapted with permission. Copyright 2015, American Chemical Society [9].

metallic T phase has been found in lithium intercalated MoS_2 [49]. Recently, theoretical calculations and experiments have shown that different stimuli [49,136,138,139], such as mechanical strain could induce phase transformation in 2D TMDs (Fig. 6c). Elastic deformations in monolayers of TMDs can be reached through tensile strain and leads to TMDs phase transformations between semiconducting 2H and metallic 1 T' structures (1 T' structures can be thought of as 1 T after a symmetry-reducing distortion), as shown in Fig. 6d and e [140,141]. Additionally, $MoTe_2$ needs much lower strain (tensile strain of 0.2%) than other TMDs for the phase transition as shown in Fig. 6a [9,136]. This strain induced phase transition may lead to controlled phase production in TMDs synthesis process.

Electronic and optical properties (Bandgap structure, absorption, exciton, photoluminescence) modification

Because of the significant effect of strain on interactions and hybridizations of the transition metal (d orbits) and sulfur or selenium (p orbits), strain is an effective strategy for engineering the bandgap structure and modulating the excitonic behavior in

2DNMs [82,142]. h-BN is a wide bandgap semiconductor, and Fujimoto et al. found that its bandgap decreases as the tensile strain increases, but increases and then decreases with the increase of the compressive strain [143]. Most of the strain engineering for the h-BN has been focused on the heterostructure of h-BN and other 2DNMs, as shown in a later section. The presence of a suitable range of bandgaps in TMDs and phosphorene opens the possibilities of photonic application in 2DNMs. The band structures of various TMDs are similar but with different effective masses and different values in bandgap [144]. MX_2 tends to be stretched and induces changes in bond lengths/angles. This deformations in bond lengths and angles play important roles in determining bandgaps, as they are directly related to the coupling of d orbitals of the M atoms and p orbitals of the X atoms [124].

MoS_2 transistors exhibits a high on/off ratio exceeding 10^8 [16],and MoS_2 photodetectors show high responsivity [145]. Structurally, the π bond-like interaction between inter atomic layers in MoS_2 is strain-sensitive and leads to the reduced bandgap under tensile strain [122,146]. Since the direct gap is only slightly lower in energy compared to the indirect gap in monolayer MoS_2 in the density function theory (DFT) calculation [147], relatively small tensile strains (~2%) can cause a direct to an indirect gap transition (Fig. 7a and b) [148,149], which was proven in photoluminescence (PL) experiments. In this case, the PL intensity of monolayer MoS_2 decreases dramatically under strain, as shown in Fig. 7c and d. Even semiconductor-to-metal transitions at ~ 8% tensile strain or at ~ 15% compressive strain were shown in calculations [59,150,151]. Further, the direct bandgap structure of monolayer and bilayer MoS_2 has been unveiled to be highly sensitive to strain experimentally with showing a red-shift (Fig. 7d, e, f and 8 a) of absorption spectrum peaks and photoluminescence (~50 meV/% strain) for the uniaxial strain [58,59]. Lloyd et al. recently reported that an up to 500 meV was tuned by large biaxial tensile strains (~5%) in a study of pressurized monolayer MoS_2 blisters. In this study, the in-plane strain has the ability to continuously and reversibly modulate the optical bandgap of monolayer MoS_2 by up to 25% [117].

Additionally, both theoretical and experimental results have shown that the shift in the photoluminescence energies of MoS_2 linearly depends upon the applied strain, therefore, the strain in MoS_2 can be quantified in PL Spectroscopy (Fig. 7c and d). Therefore, strain engineering is promising for bandgap controlling and tuning in MoS_2 for novel electronic and optoelectronic applications. The strain in MoS_2 does not affect the exciton binding (the difference between the optical bandgap and transport bandgap) in MoS_2; it is constant (~0.5 eV) under a biaxial strain up 9%. However, the energies of electron and hole decrease monotonically with the increase of the strain, as shown in Fig. 8b. Feng et al. also proposed a solar energy funnel mode for devices design based on inhomogeneous mechanical strain in monolayer MoS_2 [8].

Plentiful calculations and experiments have been performed to uncover the strain effect in other TMDs. Compressive/tensile strain reduces/increases the tungsten (W)– chalcogen (X) bond lengths, due to an increasing/decreasing coupling between the W and chalcogen atoms, which also modifies their electronic structures. Interesting, the value of the bandgap decreases monotonically under tensile strain in the monolayer of WX_2 (up to 2%), and no direct-indirect bandgap transition. However, under even smaller compressive strain in WX_2 (1% for WS_2, 1.5% for WSe_2, and 2% for WTe_2), the direct-indirect bandgap transition occurs as shown in Fig. 8c and 8d. Further, when the samples under compressive strain, their bandgaps first grow and then decrease and pass through a maximum. A strong spin splitting depends on the strain and the splitting is maintained for the valence band in all three compounds under large strain [146,152].

Monolayer and bilayer $MoSe_2$ were transferred on flexible acrylic substrates. Tensile strain induced by bending the substrates convexly resulted in a redshift of PL (-36.8 meV/% strain) (Fig. 9a). Further, a linear evaluation of intensity/polarization-dependent pattern of optical second-harmonic generation (SHG) was also proposed to detect the magnitude/direction of the strain, as shown in Fig. 9b and c. The results from the potential energy calculation and the SHG technique showed that the interlayer van der Waals forces were strong not allowing interlayer sliding during the bending of the substrate (up to 1.3%) [110]. Excitons and trions showed a similar redshift (10 meV/%) to the tensile strain in WS_2 (stretched PDMS with 12% of strain transfer efficiency) at a relatively low strain (0 to 2%) as shown in Fig. 9c; however, a wrinkle induced strain relaxation was observed under higher strain (2 to 3%) (Fig. 9c) [111]. Desai et al. experimentally demonstrated that PL intensity of the 2-4-layer WSe_2 could be significantly enhanced by tensile strain (up to 2% by substrate bending) because of the indirect-to-direct bandgap transition [125]. Because of the difference in response to strain for exciton-phonon interaction, photoluminescence and absorption, the spectrum of the A exciton becomes more narrow and symmetric for $MoSe_2$ and WSe_2 (exciton-phonon coupling reducing), unchanged for the WS_2 (weak exciton-phonon coupling at unstrained condition) and broader (exciton-phonon coupling enchantment) for MoS_2 under small tensile strain (up to 1.48%) [153]. It has been experimentally demonstrated that localized tensile strain in WSe_2 (by transferring onto nanopillars) can function as single-photon source at low temperature [154,155]. Compressive strain induces larger absorption and bandgap funnel-effect, which was significantly enhanced for the photocurrent in MoS_2 [100]. Interesting, in the vertical heterostructure of the MoS_2/WS_2, tensile strain only changed MoS_2 to indirect bandgap and WS_2's bandgap remained to be direct; however, compressive strain only tuned WS_2's bandgap to indirect and MoS_2's bandgap remained to be direct. This selective modification modified the relative PL intensity ratio of WS_2 and MoS_2 under strain direction (-7 to 20%), as shown in Fig. 9e and f [82].

Under a compressive strain, ripples form in phosphorene, and it also shows a strong anisotropy in bandgap properties, as shown in Fig. 10. For example, when ripples along the armchair direction, the bandgap changes from 0.84 to 0.51 eV for strain up to −20% and keeps almost constant at higher strain; However, for ripples along the zigzag direction, a semiconductor-to-metal transition occurs at strain ~ −30% [46]. Furthermore, either in-plane or out-of-plane strain can significantly change the bandgap of monolayer phosphorene. Specifically, a ~ − 2% in-plane strain can convert the monolayer phosphorene from a direct-gap to an indirect-gap semiconductor [35,46]. Interestingly, with sufficient expansion (+11.3%) or compression (−10.2% strains), the gap can be tuned from indirect to direct again [156]. The electron–phonon coupling is significantly enhanced by the biaxial strain due to a larger increase in density of states around the Fermi level and phonon softening in the low-frequency regime. The biaxial strain (~4%) even can increase the superconducting transition temperature from 3 K to 16 K [157].

Though many efforts have been focused on the transition from semimetal to semiconductor for 2DNMs, it is found that a semimetal-metal transition occurs when an in-plane strain is larger than 7.5% in silicene [158]. Under the strains, there is no gap opening in the silicene and germanene (Fig. 11). However, with an increase of the biaxial strain, the conduction bands at the high-symmetric Γ and M points of the first Brillouin zone shift significantly towards the Fermi level in both silicene and germanene [128]. Further, silicene and germanene show an abnormal self-doping effect under strain due to their buckled structures. Further, the relative position between Fermi level and Dirac point can be tuned by the strain in the silicene and germanene. The compressive strains (-8% for silicene and −5% for germanene) can induce a n-type doping, while the tensile strains (10% for silicene and 5% for

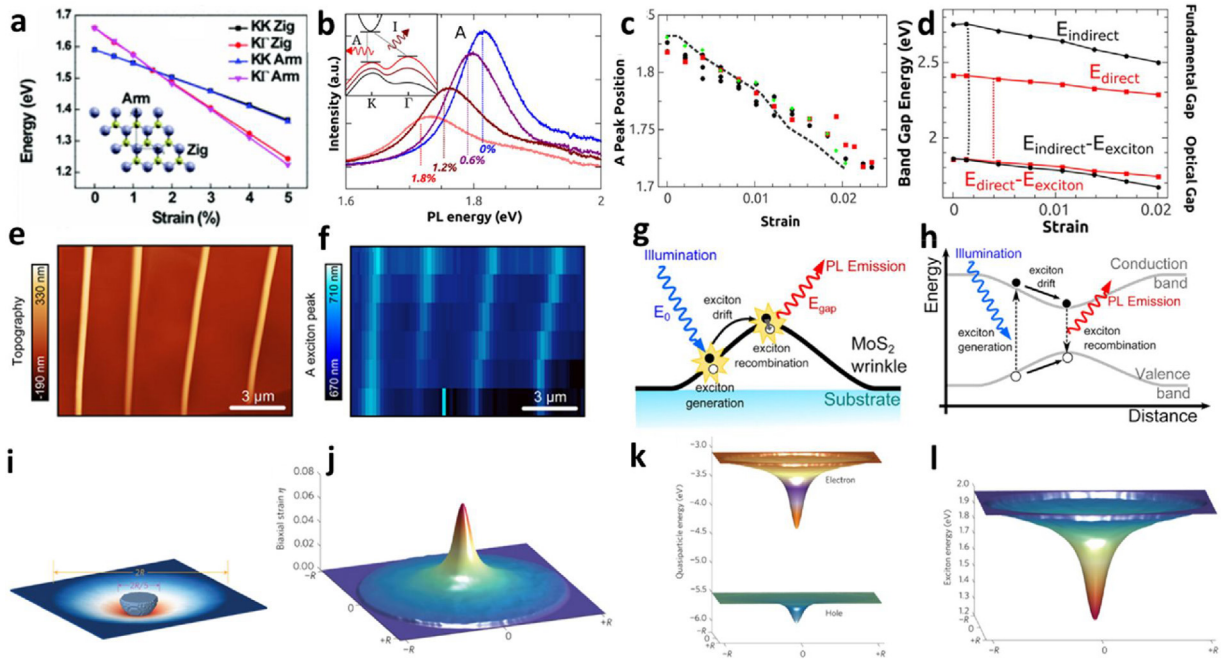

Fig. 7. Strain effect on band structure and photoluminescence in MoS_2. (a) Evolution of the direct and indirect bandgap for a MoS_2 monolayer (a) with strain applied along the zigzag and armchair directions; Adapted with permission, Copyright 2013 American Physical Society [123]. (b) PL of a representative monolayer device under strain from 0 to 1.8%; (c) Evolution of the position of the A peak of the PL spectrum (Lorentzian fits) with strain and GW_0-BSE calculations (dashed line) of expected peak, and (d) GW_0 calculations of the fundamental bandgaps of strained monolayer MoS_2. Adapted with permission. Copyright 2013, American Chemical Society [58]. (e) AFM characterization of the wrinkled MoS_2, and PL mapping (f) of the same region as (e); (g) and (h) Schematic diagram for the funnel effect in the wrinkled MoS_2. Adapted with permission. Copyright 2013, American Chemical Society [56]. (i) Schematic of monolayer MoS_2 under indentation; (j) Biaxial strain in the MoS_2; Corresponding local electron and hole energy profile (k) and local exciton energy profile (l). Adapted with permission. Copyright 2012, Nature Publishing Group [8].

germanene) can lead to the p-type doping into the these buckled two-dimensional Xene sheets (Fig. 11c) [159].

Electrical properties (Mobility, resistance, piezoelectric and flexoelectric effect)

The electrical properties of 2DNMs reflects bonding interactions and can be tuned by external strain. It is known that the strain could be applied in semiconductors to modify their electronic properties, like the mobility tuning in the silicon technology [1,2]. Therefore, it is interesting to investigate that the electrical properties modification in 2DNMs under different magnitude of strains (Fig. 12). The mobility of charge carriers in 2DNMs can also be altered by the external strain. The strain induced smaller energy gap between conductive band (relatively inert response of valance band in TMDs to strain) in Brillouin zone space can reduce intervalley phonon scattering, and in turn, increases the mobility effectively [144]. Hosseini et al. investigated the strain effect on phonon limited mobility in TMDs and indicated that tensile strain increases mobility. A significant enhancement in the mobility of single-layer $MoSe_2$ and WSe_2 is affected by a relatively small tensile strain, due to their small energy gap both at K and Q valleys. However, under a relatively small compressive strain, the lattice scattering limited mobility decreases and passes through a minimum value and then recovers with a further increase in the compressive strain [144,160]. And, the mobility enhancement effect is increase as X atom change from S to Te for WX_2 [152]. Further, strain has shown the ability to control the anisotropic free-carrier mobility in phosphorene in first-principles simulations. With the appropriate biaxial or uniaxial strain (4–6%), the preferred direction of conduction can be rotated by 90°, as a result of a switch in the energy of the lowest two conduction bands [62].

A continuous bandgap modulation and a piezoresistive effect was observed in the strain phosphorene (Fig. 12a and b). On the contrary, to strained MoS_2, tensile/compressive strain induce blue-/redshift in the absorption spectra and enlarge/shrinkage in band gap (99 ± 4 meV/% in the armchair direction and 109 ± 2 meV/% in the zigzag direction). Further, this piezo-resistive effect originates from variation in density of carriers that are thermally activated across the strain-modulated bandgap and the carriers' mobility were not affected by the strain in this experiment [161]. Magnetoresistance of $MoTe_2$ under high magnetic field showed anisotropic enhancement with tensile strain (piezoelectric substrate) in different in-plane crystallographic direction [162].

Piezoelectric (PE) effect is the ability of certain materials to generate an electric charge and potential in response to applied mechanical strain. Flexoelectric (FE) effect is an extension of the PE where PE relates uniform strain to polarization and FE relates strain gradients to polarization. The relation between polarization and strain in materials can be summarized in the equation:

$$P_i = e_{ijk}\varepsilon_{jk} + \mu_{ijkl}\frac{\partial \varepsilon_{jk}}{\partial x_l} \quad (1)$$

where e_{ijk} is the PE coefficient, μ_{ijkl} is the FE coefficient, ε_{jk} is the strain, and $\frac{\partial \varepsilon_{jk}}{\partial x_l}$ is the strain gradient [164]. These two electromechanical strain effects have wide applications in sensors, transducers, power generation and electronics [67]. For example, Wu et al. have shown the first experimental study of the PE of MoS_2 and demonstrate that only odd number of atomic layers produces oscillating piezoelectric voltage and current outputs, as shown in Fig. 12c–f [163].

Strain effect on device performance

Several studies on electronic devices performance under strain have been performed and show high mechanical robustness of 2DNMs [165]. Zhu et al. demonstrated that black phosphorus flex-

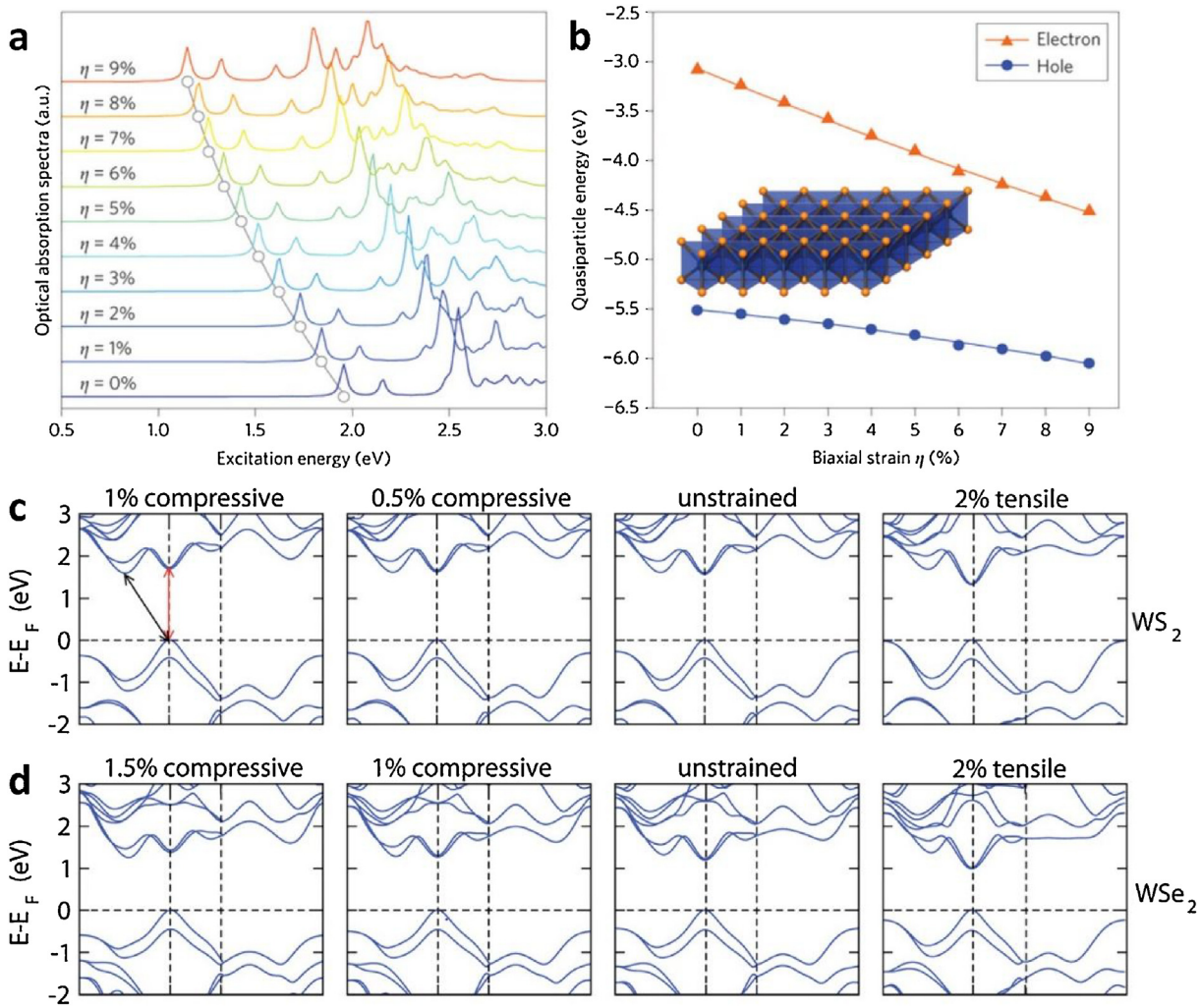

Fig. 8. Strain effect on optical absorption and carriers in MoS_2 and band structure on other TMDs. (a) Biaxial strain-dependent optical absorption spectra calculated by Bethe–Salpeter equation (BSE). (b) Biaxial strain-dependent GW quasiparticle energies for electrons and holes at the K point. Adapted with permission. Copyright 2012, Nature Publishing Group [8]. Band structures of WS_2 (c) and WSe_2 (d) under different strains. Adapted with permission. Copyright 2014, Royal Society of Chemistry [152].

ible thin film show minor degenerations under high-frequency performance under up to 1.5% tensile strain. Further the device exhibits only a small reduction in on/off ratio and mobility under 2% of uniaxial tensile strain (substrate bending, Fig. 13a) [166,167]. Das et al. reported that the flexible all-2D nanomaterials device with WS_2 channel, graphene electrode, and h-BN gate dielectric layer) has good stability under 2**%** strain [168]. It should be noticed that strain direction (tensile or compressive) is important for different devices performance enhancement. Shen et al. demonstrated that the tensile strain reduced the bandgap of WSe_2 (conduction band moves lower energy and valence band remains unchanged), which led to conduction band closed to Fermi level of electrodes (Ni) and decreased the contact (Schottky) barrier (Fig. 13b to d) [146]. This strain induced modulation of the Schottky barrier also shown in phosphorene under out-of-plane compressive strain [169]. Epitaxial grown of 2DNMs is promising for the device application, and strain in 2DNMs can be manipulated by taking advantage of the lattice mismatch between the thin film and substrate. The compressive strain was introduced in MoS_2 grown on a patterned surface with 3D cones and pyramids. This strain induced band variation in MoS_2 formed an array of "bandgap funnels" (Fig. 13g and 13 h) and facilitated the electron collection to the electrodes (Fig. 13e), which greatly enhance the photocurrent of the device, as shown in Fig. 13f [100]. On the other hand, the tensile strain will enhance the light emission resulting from reduce-bandgap induced exciton confinement. Another important note for strained 2DNMs device is that various directions, magnitude and confined dimensions of strain can be introduced into 2D thin films in the process of device preparation (especially for 2DNMs on deformable substrates). Further, the strain transfer efficiency from the substrate to the 2DNM is not always perfect. Therefore, substrate bending, stretching or compression induced strain is not always equal to the strain in 2DNMs. Further, analysis of electrical and optoelectronic performance becomes significantly complicated when including the effect of local environment (*e.g.* defects, doping, surface charges, substrate topography).

Chemical reactivity

Chemical activities are prone to influence by modification on structure of nanomaterials because of the large surface to volume ratios of 2DNMs. It has been shown that strain (or wrinkles) in graphene influence the chemical affinity and facilitates the chemical reaction [12]. The strain in MoS_2 has shown selective enhancements on the adsorption of different gas molecules (enhanced adsorption of NO and NH_3) but insensitive to the adsorption of NO_2, CO, and CO_2. This contrasting behavior may lead to new design strategies for constructing ultrahigh-sensitivity sen-

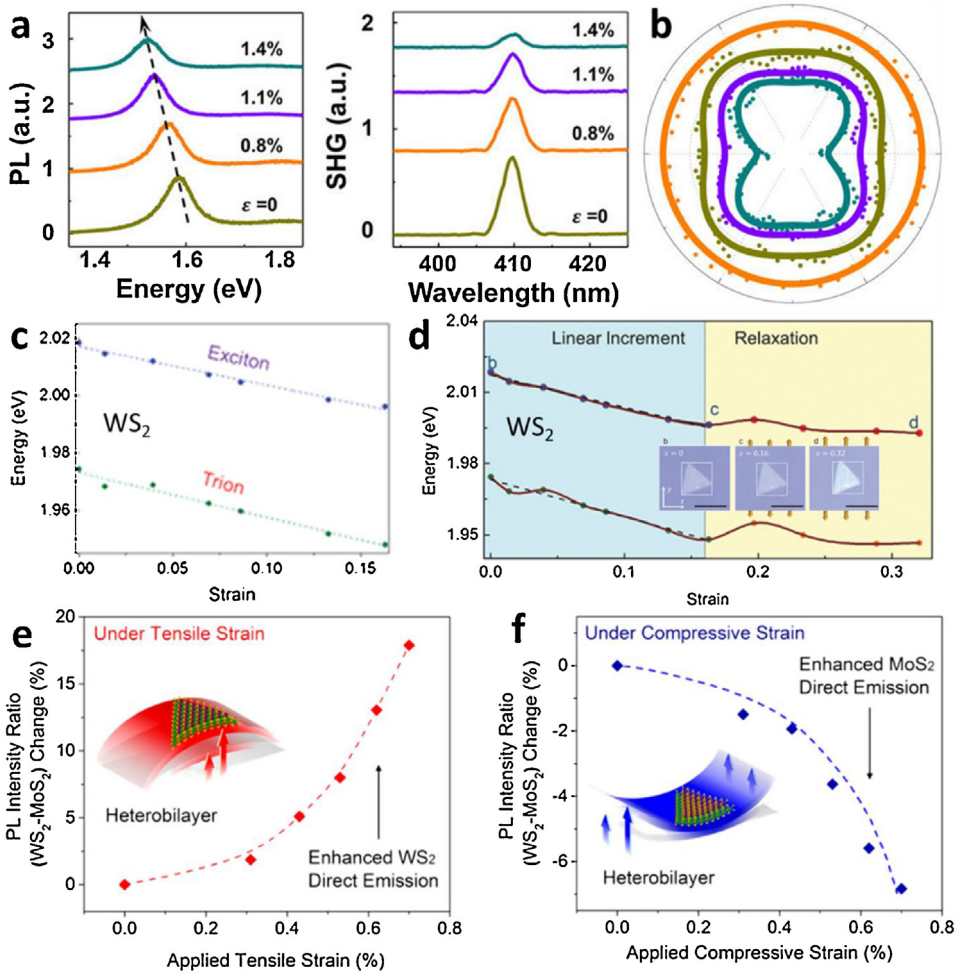

Fig. 9. Experimental studies of strain effect on optical properties and band structure of TMDs. (a) PL and second-harmonic generation (SHG) of $MoSe_2$ under different tensile strain. (b) SHG intensity dependence on Laser excitation polarization angle (respects to armchair strain) under the same series strain shown in (a). (a) and (b) Adapted with permission. Copyright 2017, American Chemical Society [110]. (c) Exciton and trion of WS_2 linear dependence on small strain, and (d) lager strain. The insert are optical images of the tensile strain applied on WS_2/PDMS structure. The e in both (c) and (d) are strains on PDMS with a ~12% of strain transfer efficiency from PDMS to WS_2 sheet. Adapted with permission, Copyright 2016, WILEY-VCH Verlag GmbH & Co. KGaA, [111], Weinheim. PL intensity ratio (WS_2 to MoS_2) dependence on (e) tensile and (f) compressive strains. Adapted with permission. Copyright 2017, American Chemical Society [82].

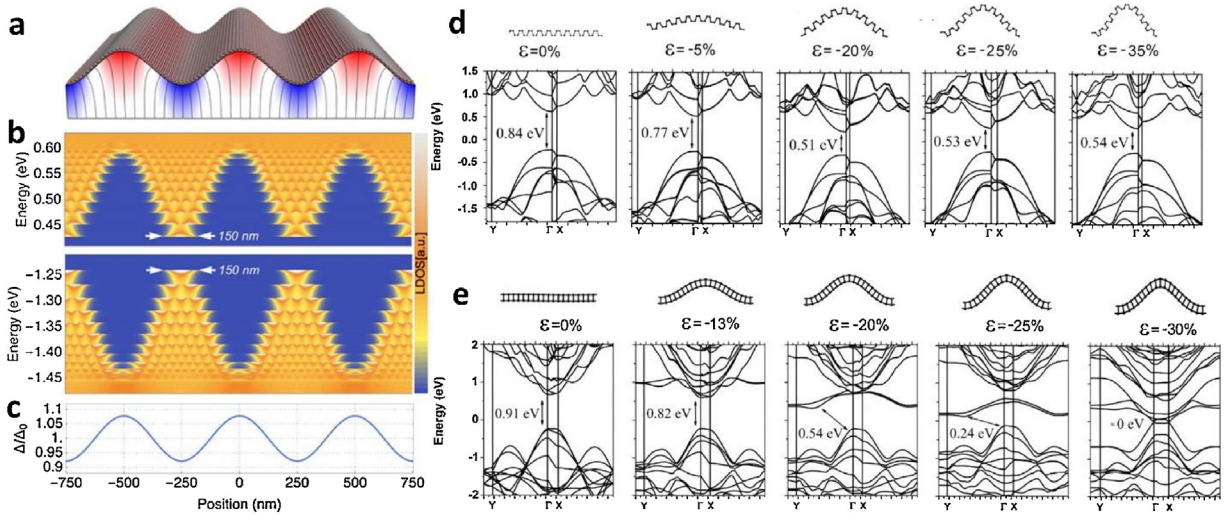

Fig. 10. Black phosphorus under compressive strain. (a) Schematic of the rippled black phosphorus monolayer on an elastomeric substrate. The ripple orientation is perpendicular to the armchair axis, and the period is 500 nm. The difference between maximum and minimum strain is 5%, red color stands for tensile strain and blue is stand for compressive strain. (b) Local density of states with several quantum-confined channels. (c) Normalized bandgap modulation along the ribbon around ±1.5% per percentage of uniaxial strain in the monolayer. Adapted with permission. Copyright 2016, American Chemical Society [57]. Strain effect on band structure in phosphorene under compressive strain along armchair (d) and zigzag (e) directions. Adapted with permission. Copyright 2016, American Chemical Society [46].

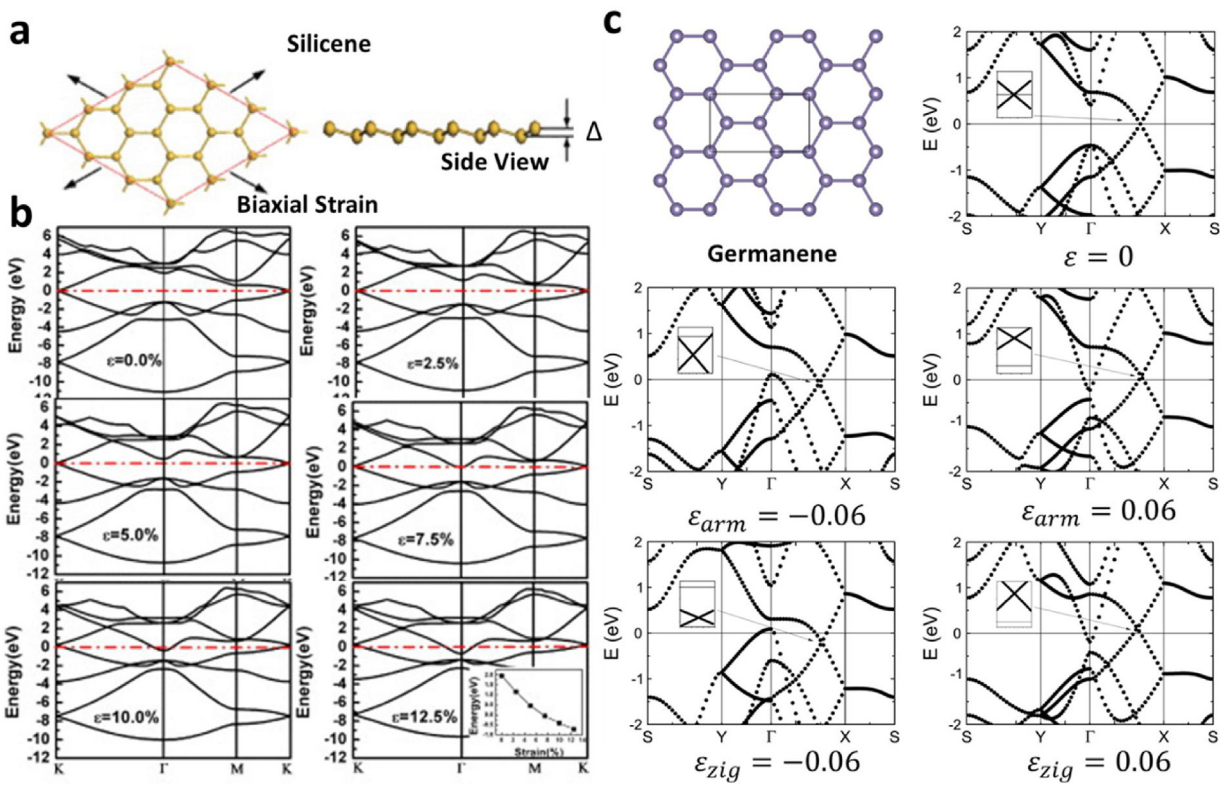

Fig. 11. Strain effect on band structure in silicene and germanene under biaxial strain. (a) Top view and side view of silicene lattice under biaxial strain and Δ is the buckling parameter; (b) Band structures of silicene with strain $\varepsilon = 0.0\%$, 2.5%, 5.0%, 7.5%, 10.0%, and 12.5%, respectively and the semimetal-metal transition occurs at 7.5% of strain. Fermi levels are all set to 0 eV; Adapted with permission, Copyright 2012, EPLA [158]. (c) Uniaxial strain-induced self-doping in germanene. Schematic of germanene atomic structure and band structure for monolayer germanene under different uniaxial strains. Adapted with permission, Copyright 2012, Elsevier Ltd [159].

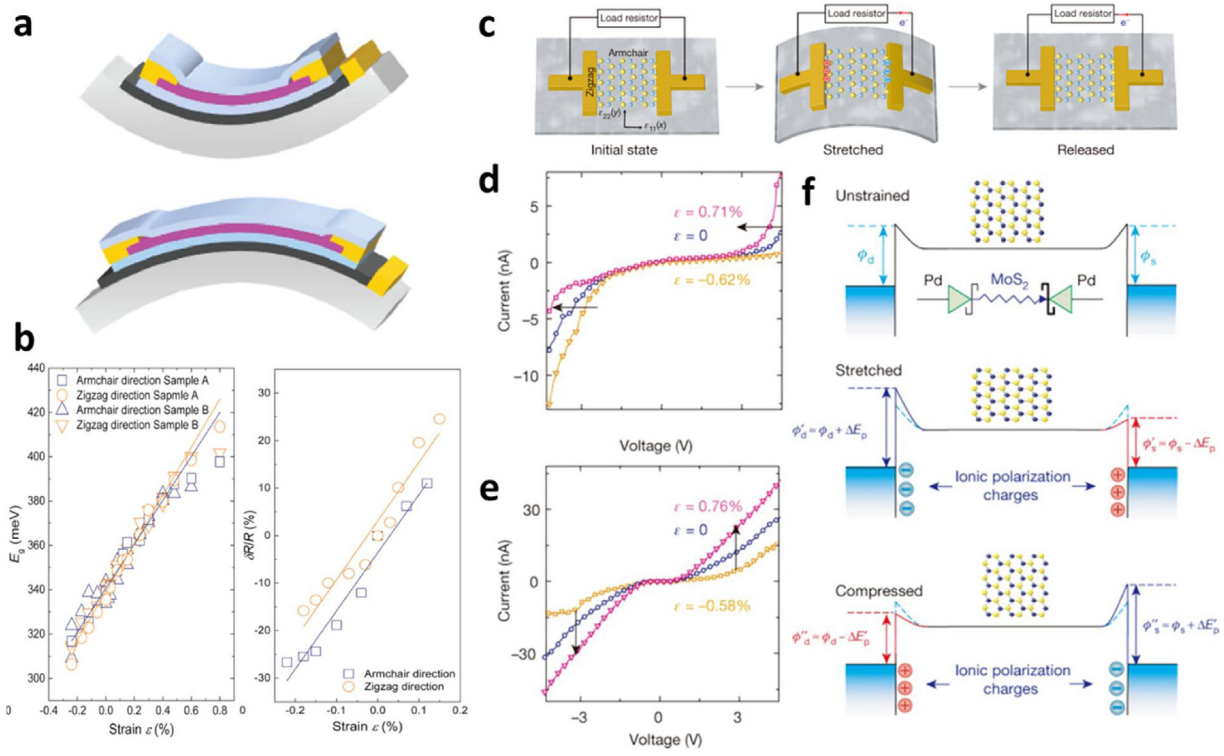

Fig. 12. Electrical properties modification of strain on 2DNMs. (a) Schematic illustration of the compressive (top) and tensile (bottom) strained phosphorene device. (b) Bandgap (left) and piezo-resistive (right) response under different strain. (a) and (b), Adapted with permission. Copyright 2017, American Chemical Society [161]. (c) Operation scheme of the single-layer MoS_2 piezoelectric device. The asymmetric (d) and symmetrical (e) modulation of carrier transport by strains under opposite drain bias. (f) Band diagrams explaining the piezotronic behaviour observed in a single-layer device as a result of the changes in Schottky barrier heights by strain-induced polarization. (c) to (f) Adapted with permission. Copyright 2014, Nature Publishing Group [163].

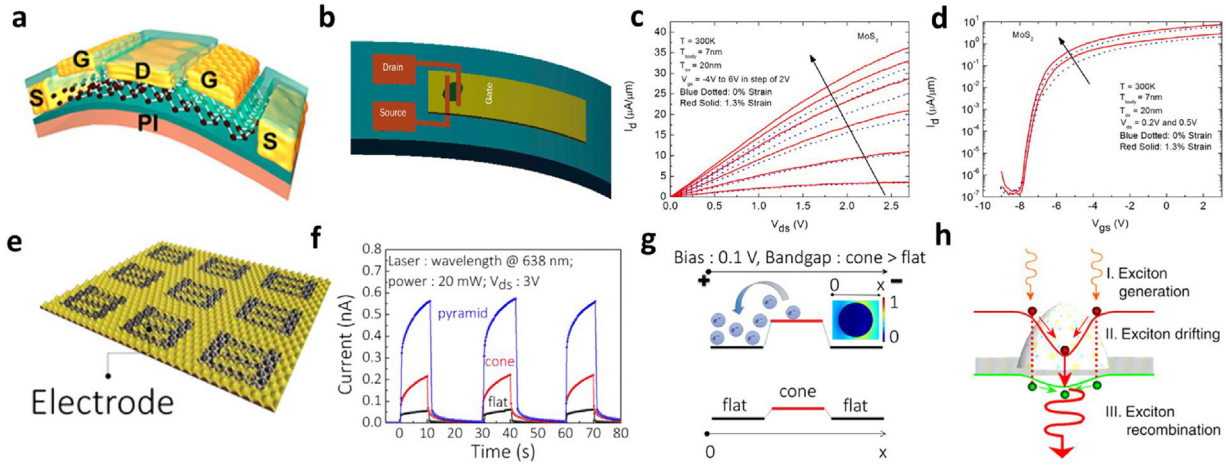

Fig. 13. Flexible electronic devices characterization and energy funneling mechanisms in strained 2DNMs. (a) Schematic illustration of the flexible phosphorene (a) and WSe_2 device (b). (a) Adapted with permission. Copyright 2016, American Chemical Society [166]. Output characteristics (c) and (d) transfer characteristics for a WSe_2 FET device under 0% and 1.3% tensile strain conditions at room temperature. (b) to (d) Adapted with permission. Copyright 2016, American Chemical Society [146]. Schematic of photodetector (e) and light response (f) of bilayer MoS_2 on surface patterned substrates. (g) Bandgap funnel effect in MoS_2 under compressive (g) and tensile strain (h). (e) to (g) Adapted with permission. Copyright 2017, American Chemical Society [100]. (h) Adapted with permission. Copyright 2015, Nature Publishing Group [170].

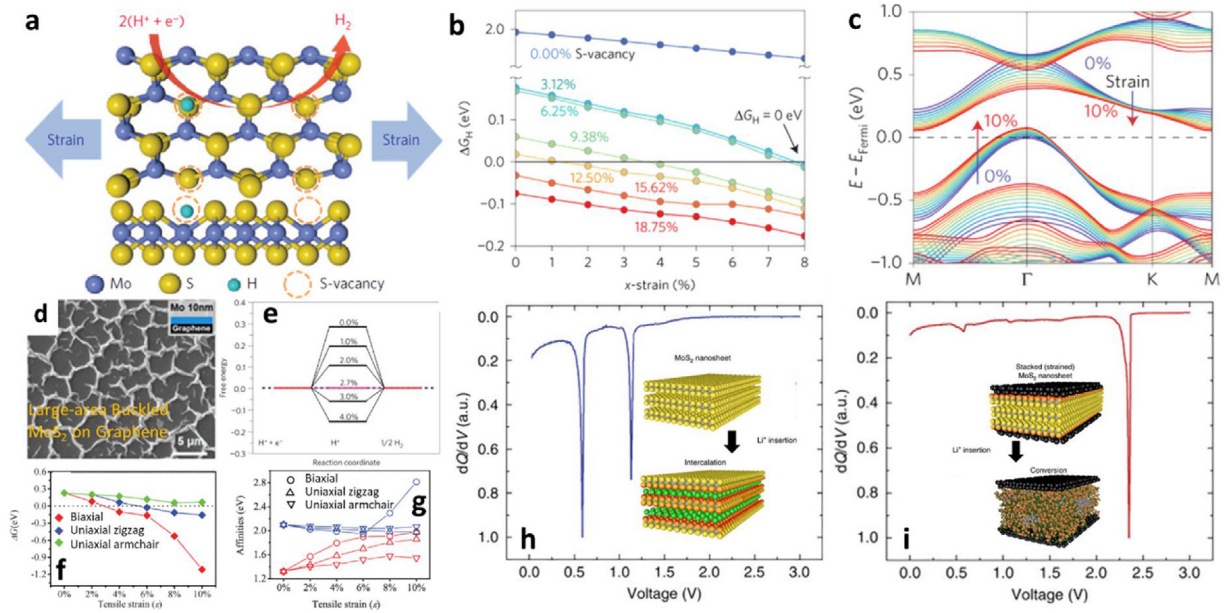

Fig. 14. Enhancement of chemical activity of strain in 2DNMs. (a) Schematic of the applied strain further tunes the HER activity of MoS_2 (S-vacancy), (b) Hydrogen adsorption free energy ΔGH evolution with strain at various S-vacancy; (c) Fine-tuning of the band structure for 25% S-vacancy under applied strain. Strain induces a narrow band gap. Adapted with permission. Copyright 2016, Nature Publishing Group [177]. (d) SEM image of buckled MoS2 films on graphene; Adapted with permission. Copyright 2016, American Chemical Society [99]. (e) The free energy of atomic hydrogen adsorption on the surface of distorted 1 T WS2 under different strain. Adapted with permission. Copyright 2013, Nature Publishing Group [176]. (f) Tensile strain dependent Gibbs free energies of H adsorption for monolayer 1 T-MoS_2; (g) Strain dependent adiabatic electron (red symbols) and proton (blue symbols) affinities of monolayer 1 T-MoS_2. Adapted with permission. Copyright 2016, Royal Society of Chemistry [173]. Normalized differential capacity measurements for MoS_2 under lithium insertion and conversion for pristine (h) and strained (i) MoS_2. Inserts are scheme shown the lithium insertion and conversion pristine (left) and strained (right) MoS_2. Adapted with permission. Copyright 2016, Nature Publishing Group [98].

sors and electromechanical devices based on strain engineering of 2DNMs [171]. Monolayer 2H-MoS_2 has been reported to be promising catalyst for hydrogen evolution reaction (HER) by introducing Sulphur (S) vacancies and strain (Fig. 14a and b). This is due to that new bands introduced by S-vacancies and reduction of the bandgap in MoS_2 under strain (Fig. 14c) [172]. The water-splitting catalytic ability of the buckled MoS_2 films showed a reduction of onset potential compared to unstrained MoS_2, as shown in Fig. 14d [46,99,159,173–175]. Electronic structure calculations show that tensile strain can activate the relatively inert inner valence electrons and enlarge the d-band exchange splitting, and further, increase the adiabatic electron affinity and decrease of the adiabatic proton affinity, and in turn, enhance the catalytic activity of the system. It is found that biaxial tensile strain can enhance the HER activity more effectively than uniaxial tensile strain, while compressive strain decreases the HER activity (Fig. 14f and g). Similar effect was also shown in the simulation of 1H-NbS_2 [173]. It has been reported that tensile strains can enhance density of states, decrease the free energy of atomic hydrogen absorption (equal to zero under 2.7% strain, Fig. 14e) and facilitate HER on zigzag-like distorted metallic 1 T WS_2 whereas tensile strains showed no enhancement for hydrogen absorption on 2H phase WS_2 (up to 4%). Furthermore, compressive strain shows trivial effect on density of states [176]. Additionally, the local strain (top and bottom peaks

of the ripples) also shows a great enhancement of chemical activities of the phosphorene [46]. The modification of the electronic properties induced by the shape anisotropy is expected to play a significant role in improving the HER catalytic activity of the MoS_2 basal plane. Comparing with two-step of lithium insertion and reaction in unstrained MoS_2, vertical heterostructure of carbon-MoS_2 showed a strain-triggered (small lattice mismatch induced compressive strain (0.1%)) chemical storage conversion without significant signature of lithium insertion, as shown in Fig. 14h and i [98].

Note to Table 2, Tensile and compressive strain

Structurally, the tensile and compressive stress can modify the bond lengths and bond angles (overlap between different orbitals) in 2DNMs. Therefore, the tensile and compressive strain is expected to have different influence on the properties. Usually, tensile strain reduces the bond strength and the lattice vibration (phonon softening). Because heat transports in solid lattice by phonons, the thermal conductivity decreases with phonon softening. Another direct effect of the phonon softening is the reduced electron-phonon coupling (interaction between electrons and lattice ions during the movement of electrons in the lattice) and increase of the carrier-mobility. Further, the bandgap and the chemical activity are governed by the overlap of the electronic orbitals, which are strongly affected by the strain direction and magnitude. For example, the energy states of the valence band and the conduction band in MoS2 originate from the 3p orbital of S atoms and 4d orbital of Mo atoms. The strain induces variations in the overlap between the 3p orbital of S and 4d orbital of Mo cause shifts in the energy states (magnitude and structure) of the valence band and conduction band [150]. Due to the Poisson effect, the tensile strain introduces compression in the out-of-plane orbitals to reduce the bandgap. Additionally, tensile strain can activate the relatively inert inner valence electrons and enlarge band splitting, and enhance the chemical activity of 2DNMs. However, the compressive strain, in most cases, exhibits a contrasting effect to the bond strength and orbital overlap in comparison to the tensile strain. This strain-direction induced difference is demonstrated in several investigations, which have been outlined in Table 2. First, different strategies are needed for the introduction of tensile and compressive strain. Several methods, for example substrate deformation, have been applied to introduce both tensile and compressive strain experimentally. Tensile strain in 2DNMs will be similar to the strain in the substrate as the 2DNMs are anchored to the substrate. However, it should be noted that compressing an anchored 2DNM on a deformable substrate does not imply the complete transfer of compressive strain to the 2DNM. The compressive deformation in 2DNMs can be compensated and partially relaxed by the formation of bucked structures, if the interfacial adhesion is not strong. The compressive and tensile strain have opposite effect on the phonon vibration and bandgap modification in 2DNMs. Tensile strain induces redshift (vibration softening) and compressive strain (vibration enhancement) induces blueshift of the Raman modes in various BN, TMDs, and phosphorene. In most 2DNMs, tensile strain reduces the magnitude of the bandgap and a compressive strain increases the bandgap; however, the strain's response to the bandgap structure in phosphorene is reversed. Furthermore, the compressive strain can result in a semiconductor-to-metal transition, but the tensile strain only reduces the bandgap to a finite value (~0.5 eV) in phosphorene [46]. The direct bandgap decreases under the tensile strain (up to 2%); however, a transition from a direct to an indirect bandgap is observed under a small amount of compressive strains in WS_2, WSe_2, and WTe_2. Tensile strain can induce a direct-to-indirect transition in MoS_2. For the electrical device performance, the mobility of single-layer $MoSe_2$ and WSe_2 increases with a relatively small tensile strain but reduces under a small compression. Therefore, in general, tensile strain induces redshift in phonon vibration, bandgap reduction and an increase of the mobility, and on the other hand, the compressive strain can induce blueshift of phonon vibration, bandgap enlargement, and mobility reduction. Various responses of 2DNMs to different strains will provide a library for further modifications of the properties to develop new concepts for strain engineering, sensing and actuating, with applications in flexible electronic devices [84,150].

Future work

Anisotropic 2DNMs under uniaxial strain

There is a gap between theoretical and experimental studies on the uniaxial strain in anisotropic 2DNMs. For the in-plane isotropic 2DNMs (graphene and TMDs), differences between the mechanical properties due to strain in the armchair and zigzag directions is small. However, there are obvious differences in the structural and mechanical properties of buckled phosphorene and Xenes for strain in the armchair and zigzag direction. In most of the theoretical calculations and simulations, strain along armchair and zigzag directions in phosphorene and Xenes were treated separately. However, precisely controlled strain-engineering along the armchair and zigzag direction is in its infancy due to the challenges in exact crystallographic strain actuation and measurements. Further, the lateral scales in experimental studies are relatively large in comparison to the crystal grains in regular samples. Strain engineering in different orientations can lead to anisotropic modifications to the structure and properties, which could play important roles in the application of flexible and logic devices [39,59,180,181].

Heterostructure of the 2DNMs in strain engineering

2DNMs based heterostructure devices are promising for high-performance flexible and transparent electronics [182,183]. On the other hand, interlayer interaction of 2DNMs heterostructures plays a great role in the performance of devices. Although the coupling has been investigated electrically and optically in various 2D heterostructures, a mechanical understanding of the interlayer coupling is indispensable but currently lacking. Further, the interfacial lattice mismatch and adhesion regulates the mechanical properties of 2DNMs heterostructures. In most cases, the strain in 2DNMs is induced through the supporting layer. Therefore, obtaining the adhesion and mechanical interactions between different 2DNMs or other substrate surfaces is essential for the straining application of 2DNMs heterostructures [53,156,183,184]. Stress applied perpendicularly or parallelly to the one-dimensional boundary of lateral heterostructures can introduce structure deformation for strain relaxation and may modify the transport (electrical and thermal), and chemical properties at the boundary. Stress (perpendicular or parallel) on a two-dimensional interface in a vertical heterostructures induces interlayer separation, rotation or shear force may show unique physical phenomena and profound applications on electronic and optical devices.

Strain engineering on 2DNMs with defect

The imperfections are regularly introduced into the 2D crystals during their synthesis, where atomic arrangements do not follow perfect crystalline patterns. Three kinds of defects can exist in two-dimensional nanomaterials: zero-dimensional point defect (vacancy, interstitial and substitutional), one-dimensional line (grain boundary) and Stone Wales defects. These defects have significant effect on the structure, physical and even chemical properties of 2DNMs, which has been covered by several previous reviews recently [172,185]. It is obvious that the defect will greatly alter the lattice and structural response of 2DNMs on strain. Further,

Table 2
Summary of strain introduction and modification of properties in 2DNMs.

2DNMs	Strain introduction	Strain type	Strain direction	Properties modification
h-BN	Simulations: DFT [121,143]	Tensile Compressive	Biaxial	Phonon vibration softening [121] Bandgap reduction [143] Phonon vibration enhancement [121] Bandgap enlargement [143]
Phosphorene	Simulations: DFT [35,62,130,157] Green's function [130] Experiments: Pre-stretched substrate [57] Substrate deformation [161]	Tensile Compressive	Biaxial Uniaxial (Z) Uniaxial (A) Uniaxial (Z) Uniaxial (A)	Thermal conductivity reduction [130] Phonon vibration softening [157] Superconducting transition temperature increase [157] Direct-indirect transition [35] Bandgap enlargement [161] Thermal conductivity enhancement (Z) [130] Phonon vibration (B2 g and A2 g) softening [126] Thermal conductivity reduction (A and Z) [130] Phonon vibration (A1g) softening [126] Bandgap enlargement [161] Conducting direction control [62] Bandgap reduction [46,161] Semiconductor-metal transition [46] Direct-indirect transition [46]
Silicene	Simulations: DFT [158] *Ab initio* [159]	Tensile Compressive	Biaxial	Semimetal-metal transition [158] Self P-type doping [159] Self N-type doping [159]
Germanene	Simulations: *Ab initio* [159]	Tensile Compressive	Biaxial	Self P-type doping [159] Self N-type doping [159]
Stanene	Simulations Molecular dynamics [77]	Tensile Compressive	Biaxial	Intrinsic thermal ripples [77]
MoS_2	Simulations: DFT [144], *Ab initio* [160] Experiments: Thermal vibrations [75] Mechanical exfoliation [81] Surface adhesion [81] Thermal expansion mismatch [84] Epitaxial grown and heterostructure [83,98,99,100,101,102,103] Chemical doping [106,107] Substrate deformation [58,59] Pre-stretched substrate [56] Pressurized blister [117] and blown bubble [119] Substrate topography modification [178]	Tensile Compressive	Biaxial & Uniaxial Uniaxial	Phonon vibration softening [56,58,59,117,123,148] Thermal conductivity [58] Direct-indirect transition [148,149] PI polarization decrease [123] Semiconductor-metal transition [59,150,151] Electron and hole energy reduction [8] Chemical activity enhancement [172,173] Carrier's mobility modification [160] Bandgap reduction [100] Phonon vibration enhancement [100,153] Bandgap enlargement [100]
WS_2	Simulations: DFT [144,152] Experiments: Substrate deformation [82,111]	Tensile Compressive	Biaxial & Uniaxial	Phonon vibration softening [82,111] Bandgap reduction [146,152] Indirect-direct transition [82,146,152] Phonon vibration enhancement [82] Chemical activity enhancement [176] Excitons and trions redshift [111] Direct to indirect transition [82]
$MoSe_2$	Simulations: DFT [144,179] Experiments: Substrate deformation [179]	Tensile Compressive	Biaxial & Uniaxial Biaxial	Carrier's mobility increase [144] Bandgap reduction [179] Exciton-phonon coupling reducing [153] Carrier's mobility decrease [144]
WSe_2	Simulations: DFT [144,152] Experiments: Substrate deformation [146] Epitaxial grown and heterostructure [105]	Tensile Compressive	Biaxial & Uniaxial	Phonon vibration softening [125] Bandgap reduction [146,152] Carrier's mobility increase [144] Exciton-phonon coupling reducing [153] Direct-indirect transition [146,152] Carrier's mobility decrease [144] Indirect-direct transition [125]

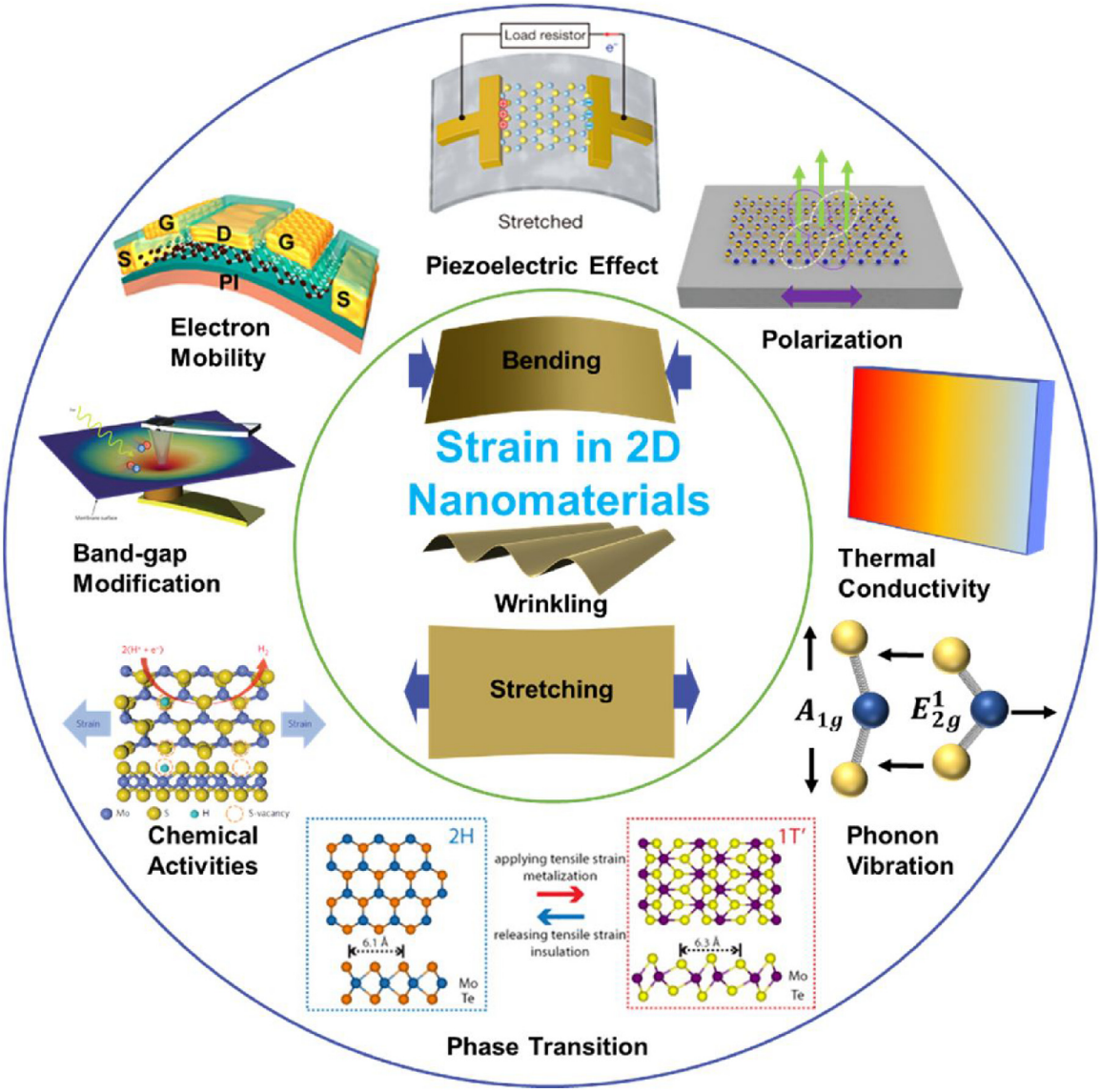

Fig. 15. Summary of strain effect in the 2DNMs. Adapted with permission [8,9,166,177,189].

physical and chemical properties of defective 2DNMs are expected to be dissimilar to ideal 2DNMs under strain; however, studies on strain engineering in defective 2DNMs are inadequate. A few experimental results have shown its promising aspect. For example, the strained MoS_2 with S-vacancies has been proved to have a significantly catalytic activity enhancement on the HER [172]. Therefore, there is a great potential of the combination of defect engineering and strain engineering in the future exploration of the application of 2DNMs.

Strain engineering in other two-dimensional thin film materials

Strain engineering in 2DNMs may provide a library of effects and phenomena to further explore and expand strategies for modification of properties to tailor applications for other thin film materials. Similar to the ability of the atomically thin 2DNMs to sustain large strain, other thin film materials (*e.g.* 2D metal-organic frameworks and perovskite thin-films) are expected to endure higher strain than their three-dimensional counterparts. For example, the mismatch of thermal expansion can induce out-of-plane compressive strain and in-plan tensile strain in organic-inorganic hybrid perovskite, which increases the ion migration and further accelerates the degradation of perovskite under illumination [186]. Few-layer (1–3) ZnO film grown on a gold surface showed a higher lattice expansion (up to 3%) and an increased band gap than buckled ZnO [187]. Blue phosphorene oxide shows a semiconductor-to-semimetal transition when the strain tensile strain increases above a critical strain [188].

Summary

With the properties of atomically-thin two-dimensional nanomaterials sensitively dependent on the lattice stresses, strain-engineering offers a platform to control the properties, even anisotropically (Fig. 15). Further, it is critical to analyze strain in 2DNM devices for their performance and behavior. This review outlines (A) lattice structure (lattice constant and thickness) and mechanical properties (Young's modulus, ultimate strength and strain, Poisson's ratio) of graphene, h-BN, phosphorene, Xenes (silicene, germanene, stanene), and TMDs (MoS_2, WS_2, $MoSe_2$, WSe_2); (B) engineering methods for strain introduction in 2DNMs: intrinsic thermal vibrations, surface adhesion, substrate deformation,

pre-stretched substrate, epitaxial growth, thermal expansion mismatch, substrate topography modification, pressurized blister, and tip indentation; (C) modification of properties due to strain in 2DNMs: structure, lattice structure and vibration, thermal conductivity, electronic bandgap, carriers' mobility, polarization, phase, piezoelectric, device performance, and chemical activities. Futuristically, it will be critical to map strain-property correlations for all the 2DNMs and develop mechanisms to directionally-control strain to rationally design 2DNM-heterostructures devices, and flexible/wearable electronics systems.

Acknowledgment

V.B. acknowledges financial support from National Science Foundation (Grants CMMI-1503681 and CMMI-1030963) and University of Illinois at Chicago. This work was performed, in part, at the Center for Nanoscale Materials, a U.S. Department of Energy Office of Science User Facility, and supported by the U.S. Department of Energy, Office of Science, under Contract No. DE-AC02-06CH11357.

References

[1] N. Mohta, S.E. Thompson, Ieee Circuits Devices Mag. 21 (2005) 18–23.
[2] M.V. Fischetti, Z. Ren, P.M. Solomon, M. Yang, K. Rim, J. Appl. Phys. 94 (2003) 1079–1095.
[3] J. Cao, E. Ertekin, V. Srinivasan, W. Fan, S. Huang, H. Zheng, et al., Nat Nano 4 (2009) 732–737.
[4] F. Guinea, M.I. Katsnelson, A.K. Geim, Nat. Phys. 6 (2010) 30–33.
[5] A.M. Smith, S. Nie, Acc. Chem. Res. 43 (2010) 190–200.
[6] E. Yablonovitch, E.O. Kane, J. Light. Technol. 6 (1988) 1292–1299.
[7] P.R. Chidambaram, C. Bowen, S. Chakravarthi, C. Machala, R. Wise, Ieee Tras. Electron. Dev. 53 (2006) 944–964.
[8] J. Feng, X. Qian, C.-W. Huang, J. Li, Nat. Photon 6 (2012) 866–872.
[9] S. Song, D.H. Keum, S. Cho, D. Perello, Y. Kim, Y.H. Lee, Nano Lett. 16 (2016) 188–193.
[10] J. Annett, G.L.W. Cross, Nature 535 (2016) 271–275.
[11] A.K. Geim, K.S. Novoselov, Nat. Mater. 6 (2007) 183–191.
[12] S. Deng, V. Berry, Mater. Today 19 (2016) 197–212.
[13] A. Molle, J. Goldberger, M. Houssa, Y. Xu, S.-C. Zhang, D. Akinwande, Nat. Mater. 16 (2017) 163–169.
[14] N. Levy, S.A. Burke, K.L. Meaker, M. Panlasigui, A. Zettl, F. Guinea, et al., Science 329 (2010) 544–547.
[15] A. Pakdel, Y. Bando, D. Golberg, Chem. Soc. Rev. 43 (2014) 934–959.
[16] B. Radisavljevic, A. Radenovic, J. Brivio, V. Giacometti, A. Kis, Nat. Nanotechnol. 6 (2011) 147–150.
[17] M. Ye, D. Winslow, D. Zhang, R. Pandey, Y. Yap, Photonics 2 (2015) 288.
[18] A. Hashimoto, K. Suenaga, A. Gloter, K. Urita, S. Iijima, Nature 430 (2004) 870–873.
[19] F. Banhart, J. Kotakoski, A.V. Krasheninnikov, ACS Nano 5 (2011) 26–41.
[20] J. Xie, H. Zhang, S. Li, R. Wang, X. Sun, M. Zhou, et al., Adv. Mater. 25 (2013) 5807–5813.
[21] K.S. Novoselov, A.K. Geim, S.V. Morozov, D. Jiang, Y. Zhang, S.V. Dubonos, et al., Science 306 (2004) 666–669.
[22] C. Lee, X. Wei, J.W. Kysar, J. Hone, Science 321 (2008) 385–388.
[23] J.S. Cameron, D.S. Ashley, J.S. Andrew, G.S. Joseph, T.G. Christopher,Nanotechnology 27 (2016), 125704.
[24] P. Nemes-Incze, Z. Osváth, K. Kamarás, L.P. Biro', Carbon 46 (2008) 1435–1442.
[25] S. Deng, E. Gao, Y. Wang, S. Sen, S.T. Sreenivasan, S. Behura, et al., ACS Nano 10 (2016) 8403–8412.
[26] J.-W. Jiang, T. Chang, X. Guo, H.S. Park, Nano Lett. 16 (2016) 5286–5290.
[27] Z. Liu, L. Ma, G. Shi, W. Zhou, Y. Gong, S. Lei, et al., Nat. Nanotechnol. 8 (2013) 119.
[28] J. Lu, L.C. Gomes, R.W. Nunes, A.H. Castro Neto, K.P. Loh, Nano Lett. 14 (2014) 5133–5139.
[29] L.H. Li, Y. Chen, Adv. Funct. Mater. 26 (2016) 2594–2608.
[30] L.H. Li, Y. Chen, G. Behan, H. Zhang, M. Petravic, A.M. Glushenkov, J. Mater. Chem. 21 (2011) 11862–11866.
[31] Q. Peng, W. Ji, S. De, Comp. Mater. Sci. 56 (2012) 11–17.
[32] K.N. Kudin, G.E. Scuseria, B.I. Yakobson,Phys. Rev. B 64 (2001), 235406.
[33] L. Song, L. Ci, H. Lu, P.B. Sorokin, C. Jin, J. Ni, et al., Nano Lett. 10 (2010) 3209–3215.
[34] L. Li, Y. Yu, G.J. Ye, Q. Ge, X. Ou, H. Wu, et al., Nat Nano 9 (2014) 372–377.
[35] H. Liu, A.T. Neal, Z. Zhu, Z. Luo, X. Xu, D. Tománek, et al., ACS Nano 8 (2014) 4033–4041.
[36] J. Jin-Wu, S.P. Harold,J. Phys. D Appl. Phys. 47 (2014), 385304.
[37] Appl. Phys. Lett. 104 (2014), 251915.
[38] Q. Wei, X. Peng,Appl. Phys. Lett. 104 (2014), 251915.
[39] T. Jiang, H. Liu, D. Huang, S. Zhang, Y. Li, X. Gong, et al., Nat. Nano 9 (2014) 825–829.
[40] G. Wang, R. Pandey, S.P. Karna, Nanoscale 7 (2015) 524–531.
[41] L. Tao, E. Cinquanta, D. Chiappe, C. Grazianetti, M. Fanciulli, M. Dubey, et al., Nat Nano 10 (2015) 227–231.
[42] R.E. Roman, S.W. Cranford, Comp. Mater. Sci. 82 (2014) 50–55.
[43] B. Mortazavi, O. Rahaman, M. Makaremi, A. Dianat, G. Cuniberti, T. Rabczuk, Phys. E Low. Syst. Nanostruct. 87 (2017) 228–232.
[44] Q.-X. Pei, Z.-D. Sha, Y.-Y. Zhang, Y.-W. Zhang,J. Appl. Phys. 115 (2014), 023519.
[45] L. Zhang, P. Bampoulis, A.N. Rudenko, Q. Yao, A. van Houselt, B. Poelsema, et al.,Phys. Rev. Lett. 116 (2016), 256804.
[46] A.A. Kistanov, Y. Cai, K. Zhou, S.V. Dmitriev, Y.-W. Zhang, J. Phys. Chem. C 120 (2016) 6876–6884.
[47] D. Jariwala, V.K. Sangwan, L.J. Lauhon, T.J. Marks, M.C. Hersam, ACS Nano 8 (2014) 1102–1120.
[48] M. Chhowalla, H.S. Shin, G. Eda, L.-J. Li, K.P. Loh, H. Zhang, Nat. Chem. 5 (2013) 263–275.
[49] R. Kappera, D. Voiry, S.E. Yalcin, B. Branch, G. Gupta, A.D. Mohite, et al., Nat. Mater. 13 (2014) 1128–1134.
[50] K. Chang, X. Hai, H. Pang, H. Zhang, L. Shi, G. Liu, et al., Adv. Mater. 28 (2016) 10033–10041.
[51] S. Bertolazzi, J. Brivio, A. Kis, ACS Nano 5 (2011) 9703–9709.
[52] Q. Peng, S. De, Phys. Chem. Chem. Phys. 15 (2013) 19427–19437.
[53] K. Liu, Q. Yan, M. Chen, W. Fan, Y. Sun, J. Suh, et al., Nano Lett. 14 (2014) 5097–5103.
[54] J. Li, N.V. Medhekar, V.B. Shenoy, J. Phys. Chem. C 117 (2013) 15842–15848.
[55] J. Kang, S. Tongay, J. Zhou, J. Li, J. Wu,Appl. Phys. Lett. 102 (2013), 012111.
[56] A. Castellanos-Gomez, R. Roldán, E. Cappelluti, M. Buscema, F. Guinea, H.S.J. van der Zant, et al., Nano Lett. 13 (2013) 5361–5366.
[57] J. Quereda, P. San-Jose, V. Parente, L. Vaquero-Garzon, A.J. Molina-Mendoza, N. Agraït, et al., Nano Lett. 16 (2016) 2931–2937.
[58] H.J. Conley, B. Wang, J.I. Ziegler, R.F. Haglund, S.T. Pantelides, K.I. Bolotin, Nano Lett. 13 (2013) 3626–3630.
[59] K. He, C. Poole, K.F. Mak, J. Shan, Nano Lett. 13 (2013) 2931–2936.
[60] L. Kang, Z. Wei-Bing, Z. Fa, Z. Fan, T. Bi-Yu,J. Phys. D Appl. Phys. 49 (2016), 185301.
[61] W. Bao, F. Miao, Z. Chen, H. Zhang, W. Jang, C. Dames, et al., Nat. Nano 4 (2009) 562–566.
[62] R. Fei, L. Yang, Nano Lett. 14 (2014) 2884–2889.
[63] E. Hanna, V. Sébastien, K. Abdelkader, L. Boubekeur, O. Hamid,J. Phys. Condens. Matter 24 (2012), 314211.
[64] J.C. Garcia, D.B. de Lima, L.V.C. Assali, J.F. Justo, J. Phys. Chem. C 115 (2011) 13242–13246.
[65] F.-f. Zhu, W.-j. Chen, Y. Xu, C.-l. Gao, D.-d. Guan, C.-h. Liu, et al., Nat. Mater. 14 (2015) 1020–1025.
[66] F. Zeng, W.-B. Zhang, B.-Y. Tang,Chin. Phys. B 24 (2015), 097103.
[67] S. Manzeli, A. Allain, A. Ghadimi, A. Kis, Nano Lett. 15 (2015) 5330–5335.
[68] Y. Yang, X. Li, M. Wen, E. Hacopian, W. Chen, Y. Gong, et al.,Adv. Mater. 29 (2017), 1604201, n/a.
[69] V. Iberi, L. Liang, A.V. Ievlev, M.G. Stanford, M.-W. Lin, X. Li, et al., Sci. Rep. 6 (2016) 30481.
[70] R. Zhang, V. Koutsos, R. Cheung,Appl. Phys. Lett. 108 (2016), 042104.
[71] W. Liu, J. Kang, D. Sarkar, Y. Khatami, D. Jena, K. Banerjee, Nano Lett. 13 (2013) 1983–1990.
[72] H. Li, G. Lu, Y. Wang, Z. Yin, C. Cong, Q. He, et al., Small 9 (2013) 1974–1981.
[73] R.E. Peierls, Ann. I. H. Poincare 5 (1935) 177–222.
[74] L.D. Landau, Phys. Z. Sowjetunion 11 (1937) 26–35.
[75] J. Brivio, D.T.L. Alexander, A. Kis, Nano Lett. 11 (2011) 5148–5153.
[76] P. Miró, M. Ghorbani-Asl, T. Heine, Adv. Mater. 25 (2013) 5473–5475.
[77] M.J. Cherukara, B. Narayanan, A. Kinaci, K. Sasikumar, S.K. Gray, M.K.Y. Chan, et al., J. Phys. Chem. Lett. 7 (2016) 3752–3759.
[78] L. Kou, Y. Ma, S.C. Smith, C. Chen, J. Phys. Chem. Lett. 6 (2015) 1509–1513.
[79] D. Nandwana, E. Ertekin, Nano Lett. 15 (2015) 1468–1475.
[80] B.C. McGuigan, P. Pochet, H.T. Johnson,Phys. Rev. B 93 (2016), 214103.
[81] S. Deng, E. Gao, Z. Xu, V. Berry, ACS Appl. Mater. Interfaces 9 (2017) 7812–7818.
[82] S. Pak, J. Lee, Y.-W. Lee, A.R. Jang, S. Ahn, K.Y. Ma, et al., Nano Lett. 17 (2017) 5634–5640.
[83] Y. Han, M.-Y. Li, G.-S. Jung, M.A. Marsalis, Z. Qin, M.J. Buehler, et al., Nat. Mater. 17 (2017) 129.
[84] P. Gerd, C.-G. Andres, B. Michele, S.Jvd.Z. Herre, A.S. Gary, K. Agnieszka, et al.,2D Materials 2 (2015), 015006.
[85] Y. Zhang, L. Zhang, C. Zhou, Acc. Chem. Res. 46 (2013) 2329–2339.
[86] S. Behura, P. Nguyen, R. Debbarma, S. Che, M.R. Seacrist, V. Berry, ACS Nano 11 (2017) 4985–4994.
[87] Z. Cai, B. Liu, X. Zou, H.-M. Cheng, Chem. Rev. (2018).
[88] M.M. Ugeda, A.J. Bradley, S.-F. Shi, F.H. da Jornada, Y. Zhang, D.Y. Qiu, et al., Nat. Mater. 13 (2014) 1091.
[89] Y. Zhang, T.-R. Chang, B. Zhou, Y.-T. Cui, H. Yan, Z. Liu, et al., Nat. Nanotechnol. 9 (2013) 111.
[90] M. Nakano, Y. Wang, Y. Kashiwabara, H. Matsuoka, Y. Iwasa, Nano Lett. 17 (2017) 5595–5599.
[91] M.M. Ugeda, A.J. Bradley, Y. Zhang, S. Onishi, Y. Chen, W. Ruan, et al., Nat. Phys. 12 (2015) 92.
[92] X. Li, W. Cai, J. An, S. Kim, J. Nah, D. Yang, et al., Science (80-) 324 (2009) 1312–1314.

[93] Y.-H. Lee, X.-Q. Zhang, W. Zhang, M.-T. Chang, C.-T. Lin, K.-D. Chang, et al., Adv. Mater. 24 (2012) 2320–2325.
[94] X. Hong, J. Kim, S.-F. Shi, Y. Zhang, C. Jin, Y. Sun, et al., Nat Nano 9 (2014) 682–686.
[95] S.M. Hu, J. Appl. Phys. 69 (1991) 7901–7903.
[96] G. Kästner, U. Gösele, Appl. Phys. Lett. 82 (2003) 3209–3211.
[97] J.L. MacManus-Driscoll, Adv. Funct. Mater. 20 (2010) 2035–2045.
[98] L. Oakes, R. Carter, T. Hanken, A.P. Cohn, K. Share, B. Schmidt, et al.,Nat. Commun. 7 (2016), 11796.
[99] S.J. Kim, D.W. Kim, J. Lim, S.-Y. Cho, S.O. Kim, H.-T. Jung, ACS Appl. Mater. Interfaces 8 (2016) 13512–13519.
[100] S.-W. Wang, H. Medina, K.-B. Hong, C.-C. Wu, Y. Qu, A. Manikandan, et al., ACS Nano 11 (2017) 8768–8776.
[101] C. Martella, C. Mennucci, E. Cinquanta, A. Lamperti, E. Cappelluti, F. Buatier de Mongeot, et al.,Adv. Mater. 29 (2017), 1605785, n/a.
[102] C. Martella, C. Mennucci, A. Lamperti, E. Cappelluti, F.B. de Mongeot, A. Molle,Adv. Mater. 30 (2018), 1705615, n/a.
[103] K.M. McCreary, A.T. Hanbicki, S. Singh, R.K. Kawakami, G.G. Jernigan, M. Ishigami, et al., Sci. Rep. 6 (2016) 35154.
[104] X. Liu, I. Balla, H. Bergeron, G.P. Campbell, M.J. Bedzyk, M.C. Hersam, ACS Nano 10 (2016) 1067–1075.
[105] S. Xie, L. Tu, Y. Han, L. Huang, K. Kang, K.U. Lao, et al., Science 359 (2018) 1131–1136.
[106] A. Azcatl, X. Qin, A. Prakash, C. Zhang, L. Cheng, Q. Wang, et al., Nano Lett. 16 (2016) 5437–5443.
[107] D. Pierucci, H. Henck, Z. Ben Aziza, C.H. Naylor, A. Balan, J.E. Rault, et al., ACS Nano 11 (2017) 1755–1761.
[108] Y.Y. Hui, X. Liu, W. Jie, N.Y. Chan, J. Hao, Y.-T. Hsu, et al., ACS Nano 7 (2013) 7126–7131.
[109] J. Quereda, P. San-Jose, V. Parente, L. Vaquero-Garzon, A.J. Molina-Mendoza, N. Agraït, et al., Nano Lett. 16 (2016) 2931–2937.
[110] J. Liang, J. Zhang, Z. Li, H. Hong, J. Wang, Z. Zhang, et al., Nano Lett. 17 (2017) 7539–7543.
[111] Q. Zhang, Z. Chang, G. Xu, Z. Wang, Y. Zhang, Z.-Q. Xu, et al., Adv. Funct. Mater. 26 (2016) 8707–8714.
[112] Z. Zong, C.-L. Chen, M.R. Dokmeci, K.-t. Wan,J. Appl. Phys. 107 (2010), 026104.
[113] H. Li, A.W. Contryman, X. Qian, S.M. Ardakani, Y. Gong, X. Wang, et al., Nat. Commun. 6 (2015) 7381.
[114] M. Rahaman, R.D. Rodriguez, G. Plechinger, S. Moras, C. Schüller, T. Korn, et al., Nano Lett. 17 (2017) 6027–6033.
[115] Y. Tan, P. Liu, L. Chen, W. Cong, Y. Ito, J. Han, et al., Adv. Mater. 26 (2014) 8023–8028.
[116] S.P. Koenig, N.G. Boddeti, M.L. Dunn, J.S. Bunch, Nat Nano 6 (2011) 543–546.
[117] D. Lloyd, X. Liu, J.W. Christopher, L. Cantley, A. Wadehra, B.L. Kim, et al., Nano Lett. 16 (2016) 5836–5841.
[118] D. Lloyd, X. Liu, N. Boddeti, L. Cantley, R. Long, M.L. Dunn, et al., Nano Lett. 17 (2017) 5329–5334.
[119] R. Yang, J. Lee, S. Ghosh, H. Tang, R.M. Sankaran, C.A. Zorman, et al., Nano Lett. 17 (2017) 4568–4575.
[120] F. Ding, H. Ji, Y. Chen, A. Herklotz, K. Dörr, Y. Mei, et al., Nano Lett. 10 (2010) 3453–3458.
[121] W. Yang, Y. Yang, F. Zheng, P. Zhang,J. Chem. Phys. 139 (2013), 214708.
[122] Y.-p. Miao, F. Ma, Y.-h. Huang, K.-w. Xu, Phys. E Low. Syst. Nanostruct. 71 (2015) 1–6.
[123] C.R. Zhu, G. Wang, B.L. Liu, X. Marie, X.F. Qiao, X. Zhang, et al.,Phys. Rev. B 88 (2013), 121301.
[124] C.-H. Chang, X. Fan, S.-H. Lin, J.-L. Kuo,Phys. Rev. B 88 (2013), 195420.
[125] S.B. Desai, G. Seol, J.S. Kang, H. Fang, C. Battaglia, R. Kapadia, et al., Nano Lett. 14 (2014) 4592–4597.
[126] Y. Li, Z. Hu, S. Lin, S.K. Lai, W. Ji, S.P. Lau,Adv. Funct. Mater. 27 (2017), 1600986, n/a.
[127] Y. Wang, C. Cong, R. Fei, W. Yang, Y. Chen, B. Cao, et al., Nano Res. 8 (2015) 3944–3953.
[128] J.-A. Yan, S.-P. Gao, R. Stein, G. Coard,Phys. Rev. B 91 (2015), 245403.
[129] T.P. Kaloni, Y.C. Cheng, U. Schwingenschlögl,J. Appl. Phys. 113 (2013), 104305.
[130] Z.-Y. Ong, Y. Cai, G. Zhang, Y.-W. Zhang, J. Phys. Chem. C 118 (2014) 25272–25277.
[131] W. Ning, X. Lanqing, W. Hui-Qiong, Z. Jin-Cheng,Nanotechnology 22 (2011), 105705.
[132] Q.-X. Pei, Y.-W. Zhang, Z.-D. Sha, V.B. Shenoy,Appl. Phys. Lett. 100 (2012), 101901.
[133] G. Zhang, Y.-W. Zhang, Mech. Mater. 91 (Pt. 2) (2015) 382–398.
[134] X. Wang, A. Tabarraei, MRS Adv. 1 (2016) 2297–2302.
[135] M. Acerce, D. Voiry, M. Chhowalla, Nat. Nano 10 (2015) 313–318.
[136] K.-A.N. Duerloo, Y. Li, E.J. Reed, Nat. Commun. 5 (2014) 4214.
[137] Y. Li, K.-A.N. Duerloo, K. Wauson, E.J. Reed,Nat. Commun. 7 (2016), 10671.
[138] D. Voiry, H. Yamaguchi, J. Li, R. Silva, D.C.B. Alves, T. Fujita, et al., Nat. Mater. 12 (2013) 850–855.
[139] H.-L. Tsai, J. Heising, J.L. Schindler, C.R. Kannewurf, M.G. Kanatzidis, Chem. Mater. 9 (1997) 879–882.
[140] D. Voiry, A. Mohite, M. Chhowalla, Chem. Soc. Rev. 44 (2015) 2702–2712.
[141] J. Berry, S. Zhou, J. Han, D.J. Srolovitz, M.P. Haataja, Nano Lett. 17 (2017) 2473–2481.
[142] W. Ju, T. Li, H. Wang, Y. Yong, X. Li, Comp. Mater. Sci. 109 (2015) 20–24.
[143] Y. Fujimoto, T. Koretsune, S. Saito, J. Ceram. Soc. Jpn. 122 (2014) 346–348.
[144] M. Hosseini, M. Elahi, M. Pourfath, D. Esseni, Ieee Trans. Electron. Dev. 62 (2015) 3192–3198.
[145] Z. Yin, H. Li, H. Li, L. Jiang, Y. Shi, Y. Sun, et al., ACS Nano 6 (2012) 74–80.
[146] T. Shen, A.V. Penumatcha, J. Appenzeller, ACS Nano 10 (2016) 4712–4718.
[147] T. Cheiwchanchamnangij, W.R.L. Lambrecht,Phys. Rev. B 85 (2012), 205302.
[148] T. Li,Phys. Rev. B 85 (2012), 235407.
[149] P. Johari, V.B. Shenoy, ACS Nano 6 (2012) 5449–5456.
[150] E. Scalise, M. Houssa, G. Pourtois, V. Afanas'ev, A. Stesmans, Nano Res. 5 (2012) 43–48.
[151] S. Yang, C. Wang, H. Sahin, H. Chen, Y. Li, S.-S. Li, et al., Nano Lett. 15 (2015) 1660–1666.
[152] B. Amin, T.P. Kaloni, U. Schwingenschlogl, RSC Adv. 4 (2014) 34561–34565.
[153] I. Niehues, R. Schmidt, M. Drüppel, P. Marauhn, D. Christiansen, M. Selig, et al., Nano Lett. 18 (2018) 1751–1757.
[154] A. Branny, S. Kumar, R. Proux, B.D. Gerardot, Nat. Commun. 8 (2017) 15053.
[155] C. Palacios-Berraquero, D.M. Kara, A.R.P. Montblanch, M. Barbone, P. Latawiec, D. Yoon, et al.,Nat. Commun. 8 (2017), 15093.
[156] H. Zongyu, H. Chaoyu, Q. Xiang, Y. Hong, L. Wenliang, W. Xiaolin, et al.,J. Phys. D Appl. Phys. 47 (2014), 075301.
[157] G. Yanfeng, W. Wenhui, Y. Fan, Y. Yugui,New J. Phys. 17 (2015), 035008.
[158] G. Liu, M.S. Wu, C.Y. Ouyang, B. Xu,EPL (Europhysics Letters) 99 (2012), 17010.
[159] Y. Wang, Y. Ding, Solid State Commun. 155 (2013) 6–11.
[160] H. Manouchehr, E. Mohammad, P. Mahdi, E. David,J. Phys. D Appl. Phys. 48 (2015), 375104.
[161] Z. Zhang, L. Li, J. Horng, N.Z. Wang, F. Yang, Y. Yu, et al., Nano Lett. 17 (2017) 6097–6103.
[162] J. Yang, J. Colen, J. Liu, M.C. Nguyen, G.-w. Chern, D. Louca, Sci. Adv. 3 (2017).
[163] W. Wu, L. Wang, Y. Li, F. Zhang, L. Lin, S. Niu, et al., Nature 514 (2014) 470–474.
[164] P.V. Yudin, A.K. Tagantsev,Nanotechnology 24 (2013), 432001.
[165] H.-Y. Chang, S. Yang, J. Lee, L. Tao, W.-S. Hwang, D. Jena, et al., ACS Nano 7 (2013) 5446–5452.
[166] W. Zhu, S. Park, M.N. Yogeesh, K.M. McNicholas, S.R. Bank, D. Akinwande, Nano Lett. 16 (2016) 2301–2306.
[167] W. Zhu, M.N. Yogeesh, S. Yang, S.H. Aldave, J.-S. Kim, S. Sonde, et al., Nano Lett. 15 (2015) 1883–1890.
[168] S. Das, R. Gulotty, A.V. Sumant, A. Roelofs, Nano Lett. 14 (2014) 2861–2866.
[169] H. Wu, X. Liu, J. Yin, J. Zhou, W. Guo, Small 12 (2016) 5276–5280.
[170] H. Li, A.W. Contryman, X. Qian, S.M. Ardakani, Y. Gong, X. Wang, et al., Nat. Commun. 6 (2015).
[171] L. Kou, A. Du, C. Chen, T. Frauenheim, Nanoscale 6 (2014) 5156–5161.
[172] L. Zhong, R.C. Bruno, K. Ethan, L. Ruitao, R. Rahul, T. Humberto, et al.,2D Materials 3 (2016), 022002.
[173] X. Chen, G. Wang, Phys. Chem. Chem. Phys. 18 (2016) 9388–9395.
[174] N. Muralidharan, R. Carter, L. Oakes, A.P. Cohn, C.L. Pint,Sci. Rep. 6 (2016), 27542.
[175] J.H. Lee, W.S. Jang, S.W. Han, H.K. Baik, Langmuir 30 (2014) 9866–9873.
[176] D. Voiry, H. Yamaguchi, J. Li, R. Silva, D.C.B. Alves, T. Fujita, et al., Nat. Mater. 12 (2013) 850.
[177] H. Li, C. Tsai, A.L. Koh, L. Cai, A.W. Contryman, A.H. Fragapane, et al., Nat. Mater. 15 (2016) 48–53.
[178] A.P. Nayak, T. Pandey, D. Voiry, J. Liu, S.T. Moran, A. Sharma, et al., Nano Lett. 15 (2015) 346–353.
[179] J.O. Island, A. Kuc, E.H. Diependaal, R. Bratschitsch, H.S.J. van der Zant, T. Heine, et al., Nanoscale 8 (2016) 2589–2593.
[180] X. Wang, A.M. Jones, K.L. Seyler, V. Tran, Y. Jia, H. Zhao, et al., Nat. Nano 10 (2015) 517–521.
[181] H. Chen, P. Huang, D. Guo, G. Xie, J. Phys. Chem. C 120 (2016) 29491–29497.
[182] J. Pu, L.-J. Li, T. Takenobu, Phys. Chem. Chem. Phys. 16 (2014) 14996–15006.
[183] A. Summerfield, A. Davies, T.S. Cheng, V.V. Korolkov, Y. Cho, C.J. Mellor, et al., Sci. Rep. 6 (2016) 22440.
[184] L. Huang, Y. Li, Z. Wei, J. Li, Sci. Rep. 5 (2015) 16448.
[185] J. Hong, C. Jin, J. Yuan, Z. Zhang,Adv. Mater. 29 (2017), 1606434, n/a.
[186] J. Zhao, Y. Deng, H. Wei, X. Zheng, Z. Yu, Y. Shao, et al., Sci. Adv. 3 (2017).
[187] J. Lee, D.C. Sorescu, X. Deng, J. Phys. Chem. Lett. 7 (2016) 1335–1340.
[188] L. Zhu, S.-S. Wang, S. Guan, Y. Liu, T. Zhang, G. Chen, et al., Nano Lett. 16 (2016) 6548–6554.
[189] W. Wu, L. Wang, Y. Li, F. Zhang, L. Lin, S. Niu, et al., Nature 514 (2014) 470.

Dr. Shikai Deng is a postdoctoral fellow at Northwestern University starting from January 2018. He received a B.E. in Chemical Engineering from Beijing University of Chemical Technology in 2012 and a Ph.D. in Chemical Engineering with Dr. Vikas Berry at the University of Illinois at Chicago in 2017. He also worked as a graduate research assistant with Dr. Anirudha V. Sumant at Center for Nanoscale Materials in Argonne National Laboratory in 2017. His research interest is on structure and properties modification of two-dimensional nanomaterials.

Dr. Anirudha Sumant is a Materials Scientist at Center for Nanoscale Materials, Argonne National Laboratory and leading the research on nanocarbon materials including CVD-diamond, carbon nanotube, graphene as well as other 2D materials. The central theme of his research direction at CNM is on developing energy efficient systems based on nanocarbon materials. He has more than 22 years of research experience in the synthesis, characterization and developing applications of carbon based materials. His main research interests include electronic, mechanical and tribological properties of carbon based materials and other 2D materials, surface chemistry, micro/ nano-scale tribology, and micro-nanofabrication. He is the author and co-author of more than 120 peer reviewed journal publications, 2 book chapters, and has 22 granted patents, 15 pending. The list of his awards includes *four R&D 100 awards*, *NASA Tech Brief Magazine Award*, three *TechConnect National Innovation Awards*, and *Pinnacle of Education Award* from Board of Governors of UChicago/Argonne LLC. He recently co-developed a nanotechnology educational kit "Next Gen STEM kit" for high school students in collaboration with United Scientific Supplies Inc. He has presented his research *via* numerous invited/keynote talks. His research in diamond materials helped in the formation of several start-up companies including NCD Technologies Inc. Bio-Oxidative Solutions Inc. He is a member of MRS, STLE and AVS.

Dr. Vikas Berry is an Associate Professor and Department Head of the Department of Chemical Engineering at University of Illinois at Chicago. Dr. Berry received his bachelor's degree from the Indian Institute of Technology-Delhi, India, in 1999, followed by a master's degree from the University of Kansas in 2003, and a doctorate degree from Virginia Polytechnic Institute and State University in 2006. Dr. Berry has made pioneering contributions in the fields of graphene and 2D materials and their Bio/Nano technologies. As an engineering faculty, Dr. Berry has earned many honors, including the NSF-CAREER Award in 2011; the Sigma Xi Outstanding Junior Scientist Award in 2010; and the Big 12 Fellowship in 2009. In 2012, Dr. Berry received a chaired-professorship appointment (William H. Honstead Professorship), which lasted till his move to UIC.